TOPICAL REVIEW

Coherent and incoherent excitations of the Gd(0001) surface on ultrafast timescales

Uwe Bovensiepen

Freie Universität Berlin, Fachbereich Physik, Arnimallee 14, 14195 Berlin, Germany

E-mail: uwe.bovensiepen@physik.fu-berlin.de

Abstract
The dynamics of collective excitations of electrons, phonons, and spins are of fundamental interest to develop a microscopic understanding of interactions among elementary excitations and of the respective relaxation mechanisms. The present work employs pump–probe investigations on the femto- and picosecond timescale to study the ultrafast dynamics of electrons, spin-waves, and phonons after intense optical excitation. The Gd(0001) surface, which serves as a model system for a ferromagnetic metal, is investigated by complementary time-resolved techniques, photoelectron spectroscopy and linear/nonlinear optical spectroscopy. The energy relaxation of hot electrons is analysed by transient changes of the electron distribution function and of the complex self-energy of the occupied component of the $5d_{z^2}$ surface state. In combination with a simplified description by the two-temperature model this analysis characterizes the optically excited state quantitatively. We analyse the mechanism that leads to a drop in spin polarization upon optical excitation, which is observed in nonlinear magneto-optics. Since the exchange splitting, analysed by photoemission, is not affected under these non-equilibrium conditions, we propose spin-flip scattering of hot electrons to be responsible. The Gd(0001) surface presents a previously unknown coupled phonon–magnon mode, which can be excited by femtosecond laser pulses. Time-resolved detection of the optical second harmonic yield separates spin dynamics from electron and lattice contributions. A coherent phonon–magnon mode at 3 THz, which is driven by electronic excitations of surface and bulk states, is observed. Time-resolved photoemission provides information on the interaction mechanism. We find that the binding energy of the surface state oscillates at the same frequency. In combination with calculations of the surface state binding energy upon lattice contraction this suggests a phonon–magnon coupling due to spin-flip scattering, in contrast to the conventional type mediated by spin–orbit interaction.

(Some figures in this article are in colour only in the electronic version)

Contents

1. Introduction

The concept of quasiparticles describes equilibrium properties and excitations of the electronic, phononic and magnetic subsystems of condensed matter [130, 9, 107]. A specific type of quasiparticles, e.g. electrons in a crystal lattice, phonons, or spin waves, can scatter with their kind of particles. The decay rate of holes has been investigated by line width measurements in photoelectron spectroscopy [137] and scanning tunnelling spectroscopy [92], or in the case of magnetic excitations by ferromagnetic resonance [131] or light scattering [153]. However, for a complete understanding many-particle interactions leading to collisions among different types of quasiparticles become important. For example, electron–phonon interaction is the cornerstone of conventional superconductivity and electron–magnon coupling has always been considered as a major relaxation channel [64]. The underlying microscopic interaction mechanisms of such coupling of different degrees of freedom in condensed matter is a current topic in solid state research and is interesting from a scientific point of view. Furthermore, it might be crucial for future applications aiming at data storage and processing devices working at THz processing rates in combination with nanoscopic spatial dimensions. Typical questions on interaction mechanisms are highlighted in the following.

(a) Carbon nanotubes, e.g., bear a great potential for nanoelectronics because metallic nanotubes are predicted to be one-dimensional quantum wires facilitating ballistic electron transport [178]. However, scattering of electrons with optical phonons represents a natural bottleneck for ballistic electron transport and might limit applications in electronic devices [83].

(b) The phenomenon of spin-transfer torque induced by spin-polarized electrical currents in magnetic multilayers [150] is discussed as a promising candidate for magnetic random access memories (MRAMs) [118]. Applications require control of spin torque transfer from an electrical current to a macroscopic magnetic moment. Recently shown microwave oscillations in nanomagnets extend the available dynamical range to GHz [90]. This behaviour has

been explained phenomenologically through spin-dependent Fermi surfaces [15]. An energy dependence in the excitation threshold of the spin excitation has been suggested [162] and refers to quasi-elastic electron–magnon scattering as the responsible elementary process.

(c) To increase the writing speed in magnetic recording techniques, understanding of fast magnetic excitation and relaxation processes on pico- and femtosecond timescales is required. This demand has recently initiated the field of ultrafast magnetization processes [76, 77], which aims at understanding the dynamical interaction principles between the spin system and further degrees of freedom on these ultrafast timescales.

The ultrafast dynamics of elementary scattering processes between electrons, phonons, and impurities on the femtosecond timescale was implicit already in an early description of electric resistance by Drude [44]. Nowadays, it is known that scattering of valence electrons with the deformation potential is responsible for electron–phonon interaction, which has been established for homopolar semiconductors [142]. Such scattering processes have been studied extensively under quasi-equilibrium conditions by, e.g., transport measurements [89]. However, only the rapid advances of time-resolved laser spectroscopy during the past decades have allowed us to disentangle the different elementary scattering mechanisms of photo-excited carriers on metal surfaces [46] in, so far, unprecedented detail. Following this approach, pump–probe experiments using femtosecond (fs) laser pulses have been carried out. In combination with complementary methods like photoelectron, scanning tunnelling, and optical spectroscopy, a profound understanding of femtosecond electron dynamics has been developed [46, 127].

The present work focuses on the Gd(0001) surface, which was found to be a favourable system to study electron–phonon, electron–magnon, and phonon–magnon interaction and the respective dynamics by fs time-resolved laser spectroscopy. The Gd(0001) surface presents a ferromagnetic and metallic model system to investigate such many particle dynamics. The surface presents an exchange-split $5d_{z^2}$ surface with the majority spin component being occupied and the minority component unoccupied, respectively. The low dimensional structure reduces the phase space available for relaxation processes. As a consequence, relaxation rates are decreased compared to the bulk, facilitating a more detailed analysis. This advantage of surfaces has led in the last decade to a comprehensive understanding of the principles governing the decay of electronic excitations in metals [46]. In semiconductor structures the dynamics proceed typically in the pico- to nanosecond regime due to the lower charge density and the smaller relaxation phase space [147, 65]. Therefore, the understanding of relaxation dynamics has been developed earlier on semiconductors employing picosecond laser pulses and is rather established nowadays. Nevertheless, the progress in understanding femtosecond dynamics on metal surfaces has also led to recent advances in the field of electron dynamics on semiconductor surfaces [175, 159].

1.1. Electronic lifetimes and electron–electron interaction

Pump–probe experiments with ultrashort laser pulses are conducted to investigate ultrafast dynamics. In these experiments, an ultrashort light pulse induces an electronic polarization in the material. Quasi-elastic scattering leads to rapid dephasing and hence absorption of light [181, 128]. Two regimes of excitation density are distinguished.

At *low* excitation densities of typically $<10^{-4}$ e$^-$/atom hot carriers decay by interaction with non-excited quasiparticles. In metallic systems, the scattering dynamics of hot electrons is governed by the high density of valence electrons, which leads to screening of the Coulomb interaction of electrons and holes in their surroundings, but also contributes to the available phase space for e–e scattering [47]. A large number of studies addressed this regime with an

emphasis on surfaces [46, 128, 174]. Theoretically, the damping rate Γ_e, i.e. the inverse lifetime τ_e, of an electron with energy $E > E_F$ is obtained in terms of the imaginary part of the complex non-local self-energy in the framework of many-body theory. The imaginary and the real part of the self-energy are evaluated in the so-called GW approximation [47]. Experimentally, the investigation of noble metal single-crystal surfaces has been very successfully carried out by the complementary methods of time- and angle-resolved two-photon photoemission (2PPE) and scanning tunnelling spectroscopy (STS). By this approach it became possible to observe electronic decay directly in the time and the momentum domain. Inter- and intraband decay processes and phonon-, step-, and adatom-induced scattering have been analysed in great detail [174]. Such studies are facilitated by the localized character of surface and image potential states on single-crystal metal surfaces. The enhanced electron density near the surface favours a decay process in the surface region, where it is not only excited but can be analysed sensitively by the employed experimental techniques. The understanding of comparable processes in bulk metal is less mature because of even faster decay and a larger phase space for e–e interaction due to the three-dimensional electronic structure [179]. An additional complication occurs from spatial relaxation due to ballistic and diffusive transport effects [101, 79]. To determine the correct lifetime of hot electrons, their contribution to the experimentally observed decay rate monitored in 2PPE within the photoelectron escape depth needs to be distinguished [102, 2]. The profound understanding of the decay of electronic excitations at metal surfaces which has been developed in close collaboration of experiment and theory in this low excitation density limit is reviewed in [46].

For *high* excitation densities ($>10^{-3}$ e$^-$/atom), as employed in the present study, interaction of the excited quasiparticles among themselves has to be considered. For an intense optical excitation a non-equilibrium distribution function of electron–hole pairs [48], as illustrated in figure 1, left, has to be taken into account. Such a non-thermal carrier distribution will redistribute its energy by electron–electron (e–e) collisions among the electron subsystem, which leads to internal thermalization among the electrons during the electron thermalization time τ_{th} (figure 1). The electron system is described by an electron temperature T_e, which is different from the lattice temperature T_l and is defined by the electron distribution function $f(E, T_e)$. The time required for thermalization depends on the excitation density. With increasing absorbed fluence τ_{th} becomes smaller because the deviation from a nascent non-thermalized distribution (figure 1, left) from a thermalized distribution diminishes and fewer scattering events are required to establish at a thermalized distribution function [48, 138]. Under excitation densities of 1 mJ cm^{-2} typical thermalization times are about 100 fs, but ballistic transport can modify this time considerably [101]. At subsequent delays, as illustrated in figure 2, left, the excess energy is transferred to the lattice via electron–phonon (e–ph) scattering, resulting in energy transfer to the lattice subsystem and 'cooling' of the electron gas (see section 1.2). In magnetically ordered systems, scattering events between hot electrons and spin waves might also redistribute the excess energy to the spin system (see section 1.3). Depending on the material under study and the optical excitation density, thermalization and cooling of the electron gas may occur on similar or separate timescales. In bulk samples the finite optical penetration depth will inevitably lead to a spatially inhomogeneous excitation. Therefore, ballistic and diffusive transport lower the excess energy density near the surface and thus contribute to the energy relaxation dynamics observed near the surface [101, 79, 102, 26].

Since the electron heat capacity is typically one to two orders of magnitude smaller compared to the lattice, T_e may reach several thousand Kelvin within the first several hundred femtoseconds after excitation while the lattice remains relatively cold [50]. This concept of separate electron and phonon temperatures provides the basis of the well known two-temperature model [6]. The evolution of both temperatures is shown exemplarily for Gd and for
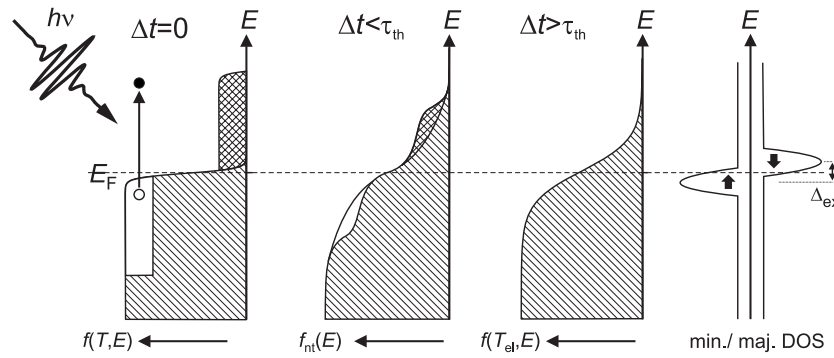
Figure 1. Schematic relaxation of the electron system in a metal after excitation of ∼0.1 e⁻/atom. Starting at a Fermi–Dirac distribution $f(E,T)$ in equilibrium, the intense laser pulse generates a strongly non-thermal electron distribution f_{nt}, which thermalizes within the thermalization time τ_{th} through electron–electron interaction and excitation of secondary electrons. Subsequently, the excess energy in the electron gas is redistributed to other quasiparticles like phonons and magnons. Diffusive and ballistic transport effects represent a competing spatial relaxation [101]. On the right, the typical electronic band structure for a ferromagnetic metal with majority and minority subbands is shown.
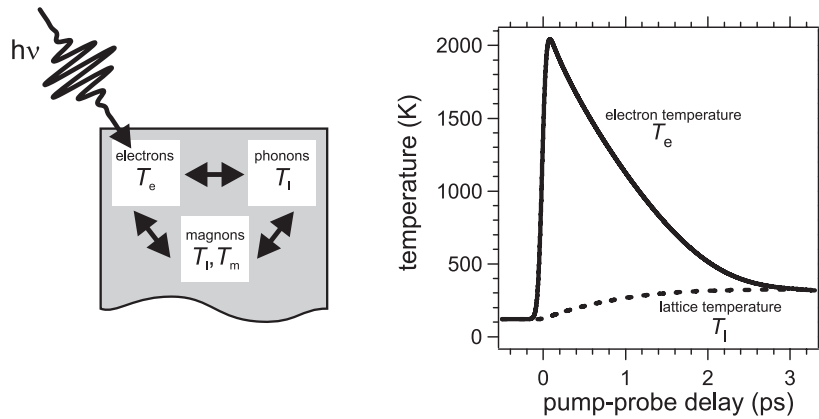

Figure 2. Left panel: schematic representation of energy redistribution among electrons, phonons, and magnons. Optical excitation drives the electron subsystem into a non-equilibrium state, which after thermalization is described by a temperature T_e. Scattering processes redistribute the excess energy among the subsystems which can be described by two separate lattice and magnon temperatures T_l and T_m, respectively, [12] or an effective T_l [105]. Right panel: transient evolution of electron and lattice temperature in Gd after optical excitation with femtosecond laser pulses for typical experimental parameters (see section 3.2).

excitation conditions employed in the present study in figure 2. The validity of this picture has been extensively analysed by experiment [101, 79, 48, 50, 61, 21, 116] and theory [138, 63]. Experimentally, the electron dynamics following optical excitation has been monitored either indirectly by a properly chosen optical response [79, 50, 61, 21] or directly by time-resolved photoemission of the photo-excited electron distribution [101, 48, 116]. From this work, it is now well established that at early times after photo-excitation the dynamics are governed by a non-thermal carrier distribution and that a description within the two-temperature model is appropriate only after electron thermalization is completed.

1.2. Dynamics of electron–phonon interaction

An electron that propagates through the crystal polarizes its environment and generates a lattice distortion. Vice versa, a deformation of the lattice modifies the electronic structure. Depending on the degree of screening of this polarization or of the induced deformation, which differs for metals and insulators, electron–phonon interaction modifies the effective mass of a respective non-interacting electron in a single-electron band structure. In the case of a free electron gas a longitudinal lattice vibration induces periodic charge accumulation at the ion cores, which will be screened by a spatial electron density that resembles the longitudinal phonon [107]. Such a transient potential deformation is represented by an inelastic coupling between electrons and phonons due to deformation potential scattering [142]. In metals, the electronic structure is renormalized near the Fermi level, where interaction with phonons influences the electronic energy [60]. In materials which exhibit a bandgap the electron–phonon (e–ph) interaction depends strongly on the character of the bonding. In the case of ionic bonding the interaction is large because of the strong Coulomb interaction and is considerably weaker for a covalent or metallic bond [91].

In this work the dynamics of (i) incoherent and (ii) coherent aspects of e–ph interaction are addressed. Here, the term coherent refers to a well defined phase of the observed signature in the time domain with respect to the instant of excitation. (i) In metals an ensemble of hot electrons relaxes through e–ph scattering and redistributes excess energy from the electron system to the lattice. Thermalization of the photo-excited electron ensemble has been addressed above in section 1.1. The dynamics of e–ph equilibration has been investigated and analysed for several metallic systems at high excitation densities ($>10^{-3}$ e$^-$/atom) in experiment [101, 79, 48, 50, 61, 21, 116] and theory [138, 63]. Typically the electron and phonon distributions have equilibrated after the first few picoseconds. As pointed out above, a description of the femtosecond-laser-excited system by the two-temperature model is appropriate only after thermalization of the electron distribution. In contrast to this requirement, e–ph interaction starts to redistribute the excess energy immediately after the optical excitation. To achieve an appropriate description, extended heat bath models have been developed that go beyond the two-temperature model by including ballistic transport effects [101, 79, 116] and non-thermalized distribution functions [101, 48, 138, 61, 63]. As demonstrated in [101] for Ru(0001), the dominating part of the excess energy can remain in the non-thermalized electron distribution up to 400 fs. We have explained our observation by a major relaxation of hot electrons through ballistic transport and a reduced e–ph interaction of the remaining non-thermalized electrons. Since various processes discussed in the present work are driven by a hot electron distribution in the high excitation limit, a prerequisite for analysis of the investigated dynamics at surfaces and interfaces is to account for these competing relaxation channels in bulk metal. Thus a description of the collective dynamics by an extended heat bath model has been developed; for details see [101]. It accounts for relaxation dynamics from diffusive and ballistic transport effects, two separate heat baths for non-thermalized and thermalized electrons, and energy dissipation to further degrees of freedom by e–ph interaction. This description is applied to Gd(0001) films investigated in this study (see section 3).

(ii) Beside such incoherent thermalization dynamics, electronic excitations in solid matter have been shown to induce coherent lattice motion. As depicted schematically in figure 3, a resonant optical excitation can launch coherent phonon wavepackets if the minimum of the excited potential surface occurs at a displaced lattice coordinate and the optical pulse is shorter than the inverse centre frequency of the phonon mode. This mechanism is referred to as displacive excitation of coherent phonons (DECP) [32, 104], which can also be considered as
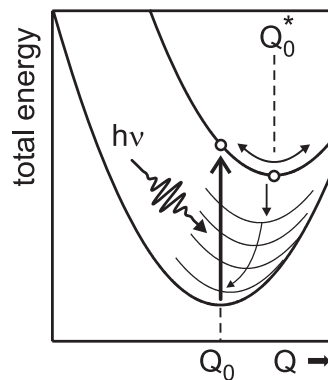
Figure 3. A schematic ground state and excited state potential as a function of a lattice distortion coordinate Q with an equilibrium lattice constant Q_0. Resonant optical excitation with a photon $h\nu$ populates the excited potential surface. Because of a displaced potential minimum Q_0^*, a phonon wavepacket is excited if the electronic lifetime τ is sufficiently long. The equilibrium potential is re-established by relaxation of the excited state.

a resonant stimulated Raman excitation [56]. For solids the absorbed energy of the laser pulse separates the ground state and the excited state potential. This is different for isolated molecules in the gas phase, where the photon energy bridges the ground state and excited state potential surface in the Frank–Condon picture. Off-resonant Raman scattering represents an alternative mechanism. In idealized cases the excitation mechanism can be recognized from the temporal phase of the coherent wavepackets [28]. In the case of DECP the displacement of the lattice coordinates occurs quasi-instantaneously on the timescale of the optical excitation (figure 3), which leads to a cosine-like variation of the transient signal. In the case of an off-resonant (impulsive) excitation an initially linear change of the transient signal is observed for the first quarter period, i.e. a sine-like variation. However, for a conclusive analysis, photon-energy-dependent effects have to be taken into account [56]. In semimetals, semiconductors, and high-T_C-superconductors, such coherent phonons have been studied extensively using femtosecond lasers by optical pump–probe experiments [32, 104, 56, 34, 72, 31, 68, 69] and by time-resolved x-ray diffraction [151, 11]. The observed frequencies are in the THz regime of optical phonons. Excitation of such coherent phonons is typically supported by a Peierls-like structural instability near the equilibrium lattice configuration as was shown theoretically [156, 157]. In bulk metals, however, such coherent phonons have been observed only very recently for transition metals [66], which might be related to the screening of holes and the resulting low excitation efficiency.

Optically induced coherent nuclear motion on surfaces has recently been reviewed comprehensively by Matsumoto and Watanabe [109]. For Cs adatoms adsorbed on Pt(111), coherent lattice dynamics have been reported [171, 170] and are attributed to a stretch vibration of Cs on Pt(111) along the surface normal. For considerably lower excitation density a continuous (or strongly damped) nuclear motion has been concluded from a dynamic binding energy stabilization of the anti-bonding resonance of Cs adsorbed on Cu(111) [129]. The Gd(0001) surface also presents such coherent lattice dynamics. The striking aspect of the observation is that this phonon-derived mode is directly coupled to the spin system. This is evident from the intensity of the nonlinear magneto-optical signal generated at the Gd(0001) surface, which oscillates in real time at the coherent phonon frequency and probes interaction mechanisms of optically excited phonons and electrons with magnons.
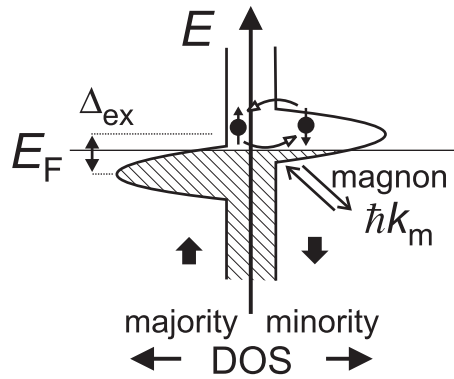
Figure 4. Electronic density of states in a ferromagnet with exchange-split subbands for majority and minority electrons. Indicated is a quasi-elastic spin-flip scattering event which is coupled to excitation or absorption of a magnon due to conservation of angular momentum.

1.3. Electron–magnon and phonon–magnon interaction

In magnetically ordered systems an excited electron does not only polarize the surrounding nuclei but can also induce an excitation of the spin system. Such interactions are based on transient changes of the exchange interaction, the anisotropic character of spin–orbit coupling, and on modifications of the magnetic moment due to e.g. spin-flip processes. The electronic structure of a ferromagnet can be described by subbands of majority and minority electrons as depicted in figure 4. Spin-flip scattering sketched in this figure is widely discussed in the literature to describe spin-dependent electrical transport [97, 88] and relaxation of low energy electrons [132–134, 80, 186]. Such a quasi-elastic spin-flip process would change the total magnetic momentum by twice the electron spin and leads to an increase in the decay rate of hot electrons due to an additional scattering channel. In a closed system the total angular momentum is conserved. Thus, such spin-flip processes are expected to be balanced by excitation (absorption) of another quasiparticle like a phonon or a magnon. Compensation of spin-flips by magnons is rather obvious since a magnon can be considered as a delocalized spin-flip. Compensation of spin-flips by phonons is well known in terms of the Einstein–de Haas effect, where reversal of magnetization in a ferromagnet leads rotation of the ferromagnetic sample. This is a direct consequence of angular momentum conservation where the change in magnetic momentum is balanced by a corresponding rotation of the whole ferromagnetic sample [154].

Individual e–e and e–ph scattering events do not change the magnetic moment because they involve only one subband. Nevertheless, the single-electron lifetime τ_{el} is longer for majority electrons than for minority ones [124, 3, 143]. This effect originates from the fact that τ_{el} depends on the phase space for e–e scattering (see section 1.1). Thus, it is the difference in the unoccupied DOS which is smaller for majority spins compared to the minority direction that is responsible for the differences in τ_{el}. Stoner excitations refer to an electron–hole pair with opposite spins for the electron and the hole. They are excited by e–e scattering of a hot majority (minority) electron with a minority (majority) electron and transfer energy within the electronic system from one subband to the other, but do not change the total magnetic momentum.

Phonon–magnon scattering has always been considered as a major relaxation mechanism in a ferromagnet [64]. For low energy excitations the linear phonon dispersion relation and the parabolic one of magnons lead to a crossover region where magnons and phonons exist at the same wavevector. Then, the true normal modes of the system are admixtures of spin

waves and phonons, which in a quasiparticle picture can be considered as a one-phonon one-magnon scattering process. However, quantitatively the amplitudes of these admixtures are determined by the coupling strength of the spin and lattice excitations, which has been attributed to magneto-elastic effects based on spin–orbit interaction [37]. This assignment is based on a comparison of Gd with a vanishing orbital momentum ($L = 0$) of the half filled 4f shell and Tb with $L = 3$ due to eight 4f electrons. In neutron scattering experiments a splitting of the Tb magnon dispersion has been observed at the values of spin wave momenta where an intersection with the phonon dispersion occurs [84, 85]. Such a splitting was not found for Gd [93], which led to the assignment of phonon–magnon interaction to spin–orbit coupling [37, 85, 167]. In the present study a coherent excitation of the spin system of the $5d_{z^2}$ surface state of Gd(0001) coupled to an optical phonon is observed. This new phenomenon suggests a phonon–magnon interaction based on a different mechanism like modification of the exchange coupling or spin-flip scattering; see section 4.

In the high excitation regime where femtosecond laser pulses create an excited electron distribution the magnetization M has been observed to be reduced within the first few hundred femtoseconds for itinerant ferromagnets by various research groups. These results have been reviewed comprehensively in [184, 94]. These observations have triggered a lot of interest in the last decade because the timescales on which changes in the magnetization are understood are limited to the nanosecond and picosecond regime where the magnetic field and the equilibrium temperature affects M. The field of magnetism on the femtosecond timescale is, thus, rather new and contains various challenging topics. Recently, not only the optically induced loss but also the onset of ferromagnetic order has been reported in the vicinity of the antiferro- to ferromagnetic phase transition in FeRh [86, 158].

The responsible microscopic mechanisms are unclear to date. Initially a three-temperature model was suggested [12, 78] to account for the electron, lattice, and spin subsystem in analogy to the two-temperature model introduced above. This concept has not become widely accepted because of its limitation to thermalized distributions. Furthermore, such a model does not contribute to the question of the underlying spin-dependent processes that are responsible for the ultrafast variation in magnetization. A momentum transfer from the spin to the orbital degree of freedom—mediated by spin–orbit interaction—has been suggested [185, 140]. Another proposed mechanism is based on Elliot–Yafet type spin-flip scattering which is mediated by a static or dynamic lattice distortion to be responsible for ultrafast variations of the magnetic moment in a ferromagnet [95]. Also the emission of electromagnetic radiation is considered [13]. Recently, the low and high density excitation regimes have been compared by means of pump–probe experiments employing spin-resolved 2PPE and linear magneto-optics in Co [35]. The authors conclude that in both experiments a pump-induced change of the total magnetization occurs, and argue along the lines of [95] that loss of magnetization requires interaction with defects or phonons. The reader should note that in the case of Gd, which has contributions to the magnetic moment from the 5d conduction band and localized 4f states, the situation might differ from itinerant ferromagnets. The reason is that spin-flip scattering in the conduction band, which is monitored in currently available set-ups, can either lower the total magnetization or be compensated by respective spin excitations in the 4f system.

The approach to investigate elementary excitations and interaction processes followed in the present study is to analyse the temporal evolution of complementary spectroscopic signatures. One question of interest is whether hot electrons interact with the spin system in a direct process like quasi-elastic spin-flip scattering, or by an indirect mechanism where at first e–ph-scattering transfers energy to the lattice and then ph–magnon coupling excites the spin system. As shown in section 3.4, a pronounced variation of the nonlinear magneto-optical signal generated resonantly by the Gd(0001) surface state, that is observed to occur

within the first 100 fs after the laser excitation, supports a direct interaction pathway. In the case of a phonon-mediated process such a transient change is expected to build up on a slower picosecond timescale.

2. Pump–probe experiments on surfaces

In this work complementary experimental methods of optical and photoelectron spectroscopy are used in pump–probe experiments to obtain a comprehensive understanding of optically excited processes and the subsequent relaxation. While optical spectroscopy is sensitive to the probability of optical transitions, photoelectron spectroscopy measures the kinetic energy and the momentum parallel to the surface of photoelectrons [81]. The energy filter in the photoelectron analyser allows the analysis of specific intermediate state energies. However, the investigation of spin-dependent properties in photoemission requires analysis of the photoelectron spin, which lowers the detection efficiency by 10^3–10^4. This might be a reason why femtosecond time-resolved photoelectron spectroscopy including spin analysis has not been demonstrated in the high excitation regime investigated here. Note that in the low excitation regime Schmidt *et al* achieved remarkable sensitivity in spin- and time-resolved 2PPE from image potential states in front of an ultrathin Fe film [143]. Linear and nonlinear optical spectroscopy, on the other hand, grants access to the spin degree of freedom by magneto-optical methods which measure the difference in light intensity or polarization upon magnetization reversal in ferromagnetic samples [14] or the optical second harmonic (SH) yield in the case of antiferromagnets [53].

The Gd(0001) surfaces have been prepared *in situ* in UHV and have been analysed with typical surface science methods like low energy electron diffraction (LEED), Auger-electron spectroscopy (AES), and photoelectron spectroscopy. It is by now well known that the growth of epitaxial lanthanide films on single-crystal metal substrates results in homogenous, clean, and well ordered lanthanide surfaces if the respective annealing temperatures are employed to avoid dewetting of the film and islands formation [10]. Electronic, structural, and magnetic properties of ultrathin Gd(0001) films have been studied widely on W(110) substrates and are by now well established [42].

2.1. Time-resolved linear and nonlinear optical spectroscopy

In centrosymmetric systems like hcp Gd(0001), separation of bulk and surface (or interface) contributions is facilitated by combining linear and nonlinear optical techniques. In linear reflection spectroscopy the signal is accumulated over the optical penetration depth of several tens of nanometres. Thus the surface contribution[1] to the reflected signal is of the order of 1%, and the bulk properties dominate. At surfaces or interfaces the inversion symmetry is broken and the electronic polarization driven by the fundamental laser field $E(\nu)$ comprises an optical second harmonic polarization $P(2\nu)$, which can be expressed by

$$P(2\nu) = \chi_{ijk}^{(2)}(2\nu, \nu, \nu) \, E_j(\nu) \, E_k(\nu), \tag{1}$$

with $\chi^{(2)}$ being the dipole second order nonlinear susceptibility tensor. In centrosymmetric materials like hcp Gd, this tensor is in the dipole approximation non-zero only at surfaces and interfaces where the inversion symmetry is broken [148]. Thus, this technique has a probing depth determined by the spatial region where the symmetry differs from bulk, which is usually a few monolayers.

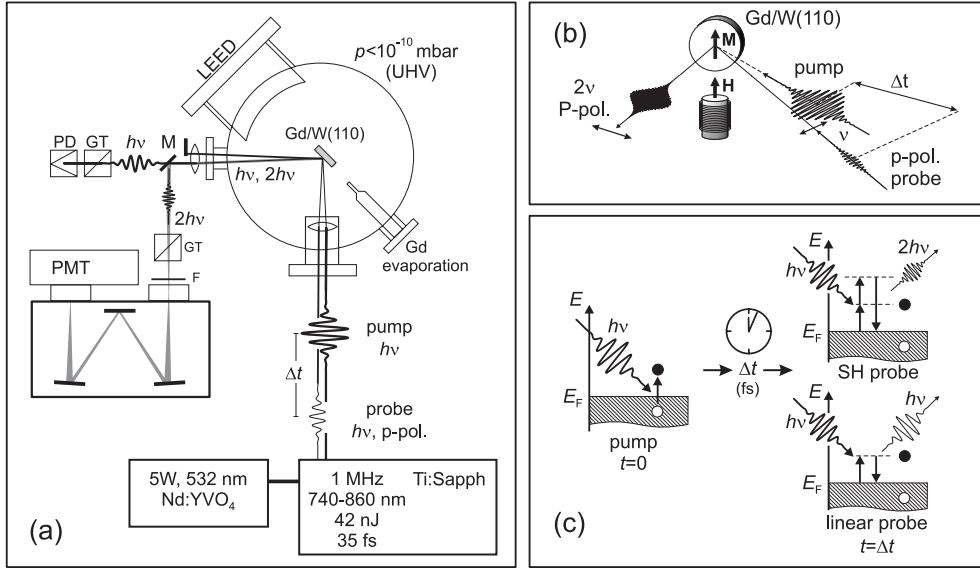[1] The term surface refers to the topmost atomic layer.

Figure 5. (a) Schematic set-up for linear and nonlinear optical pump–probe experiments on magnetic surfaces under ultrahigh vacuum conditions, which facilitate epitaxial film preparation and characterization. For detection the fundamental and second harmonic frequencies are separated by a dichroic mirror (M). The fundamental intensity of the probe pulse is detected by a photodiode after passing a polarizer (GT). The SH intensity is detected by a photomultiplier (PMT) in single-photon counting after passing a polarizer, filters (F), and monochromator to suppress remaining fundamental contributions. The pump beam is blocked after the chamber. A cavity dumped Ti:sapphire oscillator generates 35 fs laser pulses at 1 MHz repetition rate. (b) Illustration of the transversal magneto-optical pump–probe configuration. The magnetization is reversed by a magnetic field generated by an electromagnet placed below the sample. (c) Electronic processes taking part in the optical pump–probe experiment.

The SH intensity reflected from the magnetic surface is composed of two fields which behave as even or odd with respect to magnetization reversal [123]:

$$I^{\uparrow,\downarrow}(2\nu) \propto E_{\text{even}}^2(2\nu) + E_{\text{odd}}^2(2\nu) \pm 2E_{\text{even}}(2\nu)E_{\text{odd}}(2\nu)\cos(\phi). \tag{2}$$

The arrows indicate opposite magnetic field directions, and ϕ is the relative phase between even and odd SH fields. In time-resolved experiments pump-induced variations, which are sensitive to changes of the electron distribution around E_F within the photon energy, as illustrated by figure 5(c), are expressed by

$$D^{\pm}(t) = \frac{I^{\uparrow}(t) \pm I^{\downarrow}(t)}{I^{\uparrow}(t_0) \pm I^{\downarrow}(t_0)}. \tag{3}$$

Here, t_0 denotes a negative delay, i.e. before the pump pulse excites the sample. Pump-induced variations can be determined for E_{odd} and E_{even} separately, since $E_{\text{odd}} \ll E_{\text{even}}$ and $\cos(\phi) \approx 1$ [115]:

$$\Delta_{\text{even}}^{2\nu}(t) = \sqrt{D^+(t)} - 1 = \frac{E_{\text{even}}(t)}{E_{\text{even}}(t_0)} - 1 \tag{4}$$

$$\Delta_{\text{odd}}^{2\nu}(t) = \frac{D^-(t)}{\sqrt{D^+(t)}} - 1 = \frac{E_{\text{odd}}(t)}{E_{\text{odd}}(t_0)} - 1. \tag{5}$$

Unless otherwise noted, the time-dependent SH data will be presented in terms of $\Delta_{\text{even}}^{2\nu}(t)$ and $\Delta_{\text{odd}}^{2\nu}(t)$. The ratio of the even SH fields reflects the time evolution of the electron

distribution and is thus sensitive to electron and phonon dynamics. The odd pump-induced variation measures the magnetization dynamics. Further details can be found in [115].

Complementary information on the dynamics in the bulk is obtained from the transient linear reflectivity. Linear reflection of photons occurs within the optical penetration depth of Gd of about 20 nm [169][2] and thus averages over the whole film with a sensitivity that is exponentially damped with increasing distance from the surface. The pump-induced variation is determined from the reflected intensity I^ν measured with a photodiode by

$$\Delta^\nu(t) = \sqrt{\frac{I^\nu(t)}{I^\nu(t_0)}} - 1 \approx \frac{1}{2} \frac{I^\nu(t) - I^\nu(t_0)}{I^\nu(t_0)}. \tag{6}$$

The magneto-optical response was measured *in situ* in UHV using a transversal configuration. Films are magnetically saturated during the measurement by a magnetic field of 500 Oe, which was applied along the easy axis of magnetization oriented in the film plane perpendicular to the optical plane of incidence (figure 5(b)). P-polarized laser pulses of 35 fs duration at a tunable wavelength of 740–860 nm were produced by a cavity dumped Ti:sapphire oscillator. Output pulses with pulse energy of 42 nJ were split 4:1 into pump and fundamental probe pulses, respectively. Therefore, pump and probe pulses are of identical photon energy $h\nu$. The p-polarized SH intensity was separated by a dichroic mirror from the fundamental contribution. The linear reflectivity and the SH yield are monitored simultaneously by a photo-diode and a photo-multiplier tube in single-photon counting mode, respectively. For detection of the SH yield a residual intensity of the fundamental wavelength is suppressed by filters and a monochromator placed before the photo-multiplier.

2.2. Time-resolved photoelectron spectroscopy

In photoelectron spectroscopy electrons are photoemitted from the bulk and from the surface due to the kinetic energies of only a few eV and the corresponding escape depth of about 10–20 Å [182]. In order to separate bulk and surface contributions in the photoelectron spectrum, energetic separation of surface, interface, and bulk states is employed. Surface or image potential states (IPSs) are convenient for time-resolved photoemission studies because of the large wavefunction amplitude and matrix element within the probing depth of photoelectron spectroscopy. The resulting high photoelectron intensities are well suited for a time-dependent analysis. Such experiments are very sensitive to the actual surface properties, and an optimum control of the surface during the experiment is required. This is achieved under UHV conditions, which furthermore allow a systematic variation of surface properties.

Direct and inverse photoelectron spectroscopies facilitate experimental access to the static electronic structure of condensed matter [81]. In addition, femtosecond time-resolved investigations in combination with first principle calculations of electronic excitations led to a profound understanding of electronic relaxation processes at metal surfaces during the last decade [46, 128, 174]. In the present work two time-resolved photoemission methods have been employed. (i) In time-resolved single-photon photoemission (TRPE) an intense pump pulse $h\nu_1$ excites the electronic system as indicated in the bottom panel of figure 6(b). A time-delayed probe pulse $h\nu_1$ with a photon energy larger than the work function, which is the energy difference between the Fermi level and the vacuum energy $\Phi = E_{\text{vac}} - E_{\text{F}}$, monitors transient changes of the electron distribution and binding energies. The initial state level is determined from the analysed kinetic energy of the photoelectron by subtraction of the probe

---

[2] Note that experimental values of the imaginary refraction index k which are reported for $\lambda = 800$ nm vary from 1.55 to 3.46. This results in an optical penetration depth of $\delta = \lambda/(4\pi k)$ between 41 and 18 nm.
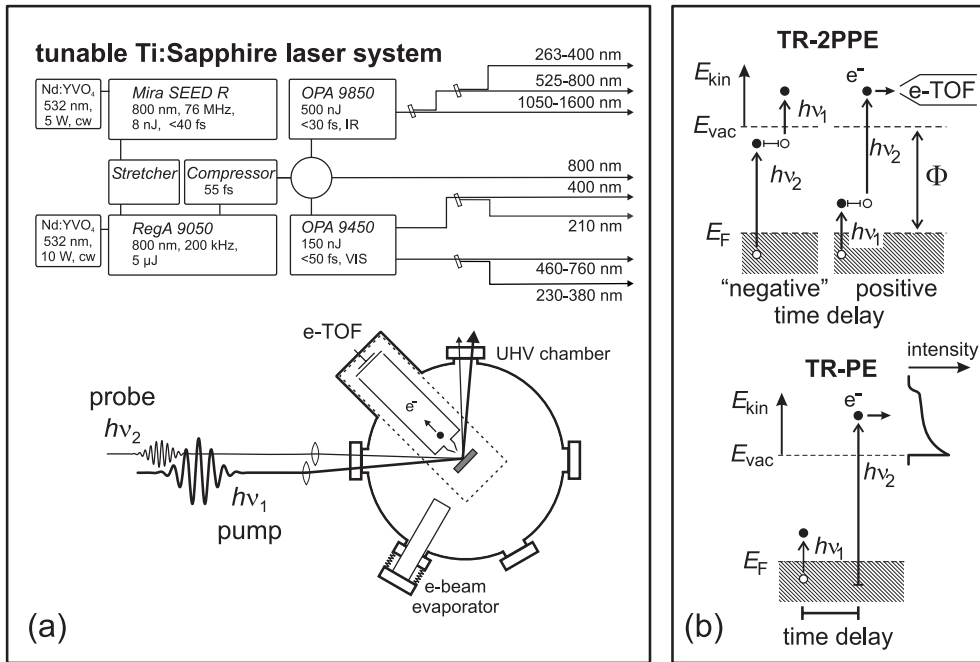
Figure 6. (a) Schematic experimental set-up for time-resolved photoemission and two-photon photoemission. To achieve a wide tunability of femtosecond laser pulses, a regeneratively amplified (RegA) laser system operating at 20–300 kHz is used. Its output drives two optical parametric amplifiers (OPAs), which generate a signal output in the VIS or IR range. Frequency doubling or quadrupling of the OPA and RegA laser pulses covers a wide spectral range as indicated. Pairs of laser pulses are time delayed with respect to each other and are focused onto the single-crystal surface in the UHV chamber. The kinetic energy of photoelectrons is analysed by an electron time-of-flight spectrometer (e-TOF). (b) Illustration of time-resolved photoemission (TRPE) and two-photon photoemission (TR-2PPE). In TRPE the photon energy of the probe pulse $h\nu_2$ exceeds the work function Φ and monitors changes in occupied and unoccupied states simultaneously, however at very different count rates. In TR-2PPE, only the photon energy sum of both employed photons exceeds the work function and either the IR ($h\nu_1$) or the UV photon ($h\nu_2$) can be used for excitation of the system. The subsequent pulse probes the excited state. Consequently, the energy level of the intermediate state which is analysed depends on the sequence of the laser pulses.

photon energy.

$$E - E_{\mathrm{F}} = E_{\mathrm{kin}} + \Phi - h\nu_2. \tag{7}$$

The maximum kinetic energy in the spectrum originates from electrons excited by $h\nu_2$ from E_{F}. The low energy cut-off in the spectrum is generated by electrons that just overcome the work-function barrier; see figure 6(b) (bottom).

Two-photon photoemission (2PPE) spectroscopy is a second order process. Electrons are excited by photon absorption from below the Fermi level to bound intermediate states below E_{vac}. These hot electrons are excited by absorption of a second photon from the same laser pulse or—in time-resolved 2PPE—from a second, time-delayed pulse into the continuum of final states as illustrated in the top panel of figure 6(b). This method probes simultaneously occupied and unoccupied states. An assignment of peaks observed in the spectrum to intermediate states above E_{F} or to initial states below E_{F} is carried out by photon-energy-dependent studies [51]. In a case where $h\nu_2 = 2h\nu_1$, generated by frequency doubling in a nonlinear crystal, the kinetic energy of a peak originating from an occupied

state would disperse with three times the photon energy variation because pump and probe pulses both affect the kinetic energy. For an unoccupied intermediate state only the probe step would change E_{kin}. Consequently, the kinetic energy would shift linearly with $h\nu_1$ or $h\nu_2$, respectively, depending which laser pulse is probing. Depending on the sequence of pulses, either unoccupied states close E_F which are excited by $h\nu_1$ or closer to E_{vac} are probed. Further details on 2PPE can be found in overview articles by Fauster and Steinmann [51], Petek and Ogawa [128], and Weinelt [174].

For time-resolved photoemission studies a widely tunable femtosecond laser system has been set up, which is based on the commercially available Coherent RegA 9050, see figure 6(a). This regeneratively amplified Ti:sapphire laser generates femtosecond laser pulses of typically 4 μJ energy per pulse at a repetition rate of 300 kHz, 800 nm wavelength, and 55 fs pulse duration. Tunability of the fundamental pulse is very limited (790–840 nm). Nonlinear optical parametric processes [148] are employed in optical parametric amplifiers to produce tunable femtosecond laser pulses in the visible (VIS) and in the infrared (IR) spectral region. Further frequency doubling (quadrupling in the case of the IR OPA) transfers the tunability into the ultraviolet (UV), respectively. Quadrupling of the fundamental pulse results in a UV pulse with 6 eV photon energy, which is used for TRPE.

Time-delayed pairs of laser pulses with photon energies selected for the problem under study are focused into the UHV chamber onto the sample surface. The kinetic energy of photoelectrons is analysed in normal emission by an electron time-of-flight spectrometer (e-TOF) based on a drift tube with a length of 300 mm. The spectrometer acceptance angle is 7°. The laser repetition rate matches well the time window required to analyse the electron flight times in the e-TOF of $\leqslant 10^{-6}$ s. To avoid limitations in count rate in the time-of-flight detection, a time-to-digital converter that analyses multiple events per laser pulse is employed. Care has been taken to avoid space charge effects among photoelectrons that would distort the spectra. An overview of these space effects has been given by Gilton *et al* [58]. This is especially important for pump and probe pulses in TRPE experiments in the high excitation regime, where count rates up 1 MHz, i.e. five events per laser pulse, can easily be generated. To identify the space charge limit the fluence of pump and probe laser pulses is varied and shifts in the kinetic energy of the Fermi edge signature are analysed. For effects of the UV probe pulse only spectra are compared to a direct photoemission spectrum recorded at low count rates < 50 kHz. This procedure is a prerequisite to perform time-resolved photoemission experiments because the photoemission yield induced by the probe pulse in direct photoemission is of the same order as the yield generated by multiphoton processes of the 1.5 eV pump beam. The experiments reported in the following show a maximum shift due to space charge of 10 meV kinetic energy compared to the low fluence limit, which is comparable to the energy resolution of the electron time-of-flight spectrometer.

The spectrometer's energy resolution has been determined as follows. The width of the low energy cut-off of the PE spectrum which is unaffected by the laser pulse band width is 10 meV at a kinetic energy of 0.25 eV. Due to the time-of-flight technique the energy resolution depends on the kinetic energy and is estimated to be 13 meV at typical kinetic energies of 1 eV. This has been verified by analysis of a photoelectron spectrum around E_F at 30 K. A convolution of the distribution function with the laser pulse band width and the spectrometer resolution reproduces the measured spectrum and is in agreement with the energy resolution determined from the cut-off in the spectrum.

The absorbed fluence determines the optical excitation density. It is determined by measuring the power of the laser beam reflected from Gd(0001) and by analysis of the laser beam focus at a CCD camera. The latter has been positioned *ex situ* in such a way that it corresponds to the distance between sample surface and focusing lens [101].

3. Incoherent equilibration dynamics of the electron, spin, and lattice subsystems

3.1. Equilibrium properties and preparation of Gd(0001)

This work represents the first experimental investigation of femtosecond spin dynamics of pure rare earth ferromagnets. It aims at an understanding of elementary spin-dependent scattering events by time-resolved investigations. The starting point is set by the current knowledge of spin-dependent processes under equilibrium conditions. For example, the mechanism which is responsible for the reduction of the magnetization M with increasing temperature T in ferromagnets up to the Curie temperature T_C has been debated for decades [30] and two simple model descriptions are widely discussed. The *Stoner model*, which is appropriate for delocalized spins, predicts a decrease in the exchange interaction with T proportional to $M(T)$. For localized spins, on the other hand, fluctuations and excitations of magnetic moments lower M, while the exchange interaction is not affected by an increase in T. This is referred to as *spin mixing behaviour* following the Heisenberg model of localized spins and is beyond a single-particle description [139]. Neutron scattering experiments of 3d itinerant ferromagnets like Fe, Co, and Ni provide evidence for spin waves and local magnetic moments even above the Curie temperature T_C, which suggests a localized character of spins [27]. However, a Stoner-like collapse of the exchange splitting of majority and minority subbands at T_C observed in photoemission emphasizes their itinerancy, because the quasi-free valence electrons average over spatial fluctuations of the local spin density [168, 59]. It has been concluded that neither of these simple models accounts for the temperature-dependent properties since 3d spins exhibit localized and delocalized contributions in parallel [4]. Both have been included in a generalized Hubbard model successfully [119].

In lanthanides the magnetic moment μ is dominated by the spins of 4f electrons. These are localized at the ion core, polarize the valence band, and generate an itinerant contribution to μ. In Gd the exchange splitting of valence electrons Δ_{ex} is reduced with increasing temperature, but remains finite above T_C while the spin polarization vanishes [139, 108]. The equilibrium properties of the exchange-split $5d_{z^2}$ surface state of Gd(0001) have been studied extensively [108, 100, 177, 19, 52, 98, 136]. It exhibits a finite exchange splitting at T_C of $\Delta_{ex} = 0.4$ eV [19]; see also figure 8 discussed below. Therefore, the surface state exhibits an analogous behaviour to bulk Gd. This feature, which is not described by the Stoner model, can be conceived by taking the small coherence length of the 5d electrons into account, which can be smaller than regions of spin fluctuations in the thermally activated system [139, 100]. Overall, in Gd neither Stoner behaviour nor spin mixing prevails [108, 177], and a complete understanding of magnetic quasiparticle excitations is challenging to date.

Due to the reactivity and the resulting contamination of lanthanide single crystals, it is by now well established to prepare lanthanide surfaces by epitaxial growth of films on single-crystal metal substrates under UHV conditions [7]. The substrate employed here is W(110). Adsorption of Gd atoms evaporated from an electron-beam-heated crucible leads to rough and disordered films. Annealing to thickness-dependent temperatures between 500 and 900 K for 10–100 monolayer (ML) thickness [10] results in a well ordered film with a smooth (0001) surface [160]. If annealed to higher temperatures, the film breaks up and forms hexagonal-shaped islands with 200 nm lateral extension. In the present study, films of 30–60 ML have been grown in UHV (background pressure $p < 1 \times 10^{-10}$ mbar) at room temperature with subsequent annealing.

Gd is ferromagnetic at temperatures below $T_C = 293$ K for bulk and is lowered due to finite size effects for film thicknesses below 25 ML [49]. The magnetic moment of Gd of 7.55 μ_B/atom [45] is highly localized to the 4f shell, which is occupied by seven electrons that generate a magnetic moment $\mu_{4f} = 7 \mu_B$. Polarization of the conduction band
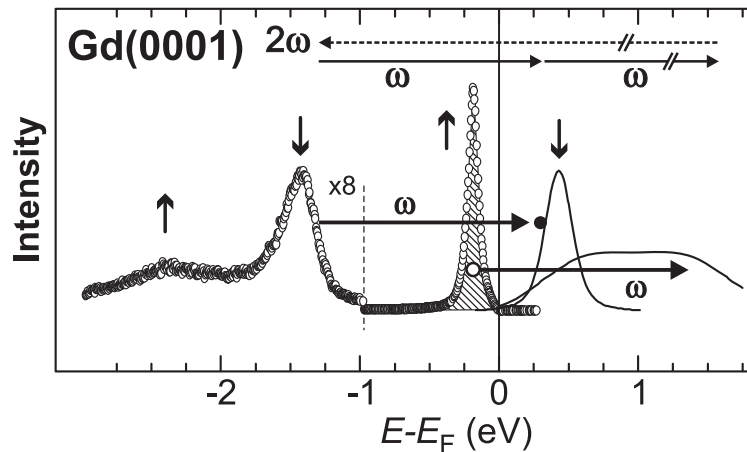
Figure 7. Electronic structure of Gd(0001) near the Fermi level studied by photoelectron spectroscopy in normal emission at $T = 90$ K. Vertical arrows indicate the spin direction (↑ majority, ↓ minority). Peaks at energies < -1 eV represent occupied bulk states; the states at -0.2 and 0.4 eV are the occupied and unoccupied components of the surface state, respectively. Occupied states have been measured by direct photoemission using 36 eV photons from a synchrotron [114]. Data of the unoccupied surface state have been taken by STS [136]. The broad spectral contribution in the unoccupied region reflects unoccupied bulk states which are also spin-split according to theory [98]. This is not obvious from the inverse PE data taken from [177] but is discerned by spin-resolved inverse photoemission by Donath *et al* [43]. Horizontal arrows indicate optical transitions driven by the Ti:sapphire laser at $h\nu = 1.5$ eV. SH generation proceeds resonantly enhanced through the unoccupied surface state component as an intermediate state (top horizontal arrows) [113]. Reprinted with permission from [115]. Copyright 2003 American Physical Society.

leads (i) to indirect exchange interaction (RKKY interaction), which is responsible for the ferromagnetic order in the material, and (ii) to an itinerant contribution to magnetic moment of $\mu_{5d6s} = 0.55 \, \mu_B$. Consequently, the electronic structure of the 5d6s valence band presents subbands of majority and minority spins which have been investigated by photoemission [146], spin-resolved photoemission [108], and density functional theory [98]. The Gd(0001) surface exhibits a localized d_{z^2} surface state, which has been studied extensively by experiment and theory [108, 100, 177, 19, 52, 98, 136, 43]. The electronic valence structure at the Gd(0001) surface at the $\overline{\Gamma}$-point near the Fermi level is given in figure 7.

The Curie temperature of the Gd(0001) surface has been controversial for more than a decade owing to reports of a surface T_C enhancement by 15–85 K compared to the bulk value. Other studies indicate that the surface transition is ordinary, with the same T_C for surface and bulk; see [8] and references therein. Meanwhile, a consistent picture has developed. In scanning tunnelling spectroscopy it is observed that the exchange splitting of the surface state Δ_{ex} decreases with temperature from 0.7 eV at 10 K to 0.4 eV at 290 K, i.e. it remains finite at the Curie point [19]. The surface magnetization, which has been measured by spin-polarized secondary electron emission, vanishes at the bulk T_C [8]. Furthermore, spin-polarized photoemission of the occupied component of the surface state has shown that the spin polarization vanishes at T_C, albeit the exchange splitting remains finite [108]. The current understanding is that the temperature-dependent spin polarization of the Gd(0001) surface state does not follow a pure Stoner behaviour[3]. Therefore, it has been concluded that

---

[3] The Stoner behaviour is characterized by a decrease in exchange splitting with increasing temperature proportional to the magnetization M and is derived for idealized delocalized spin densities.
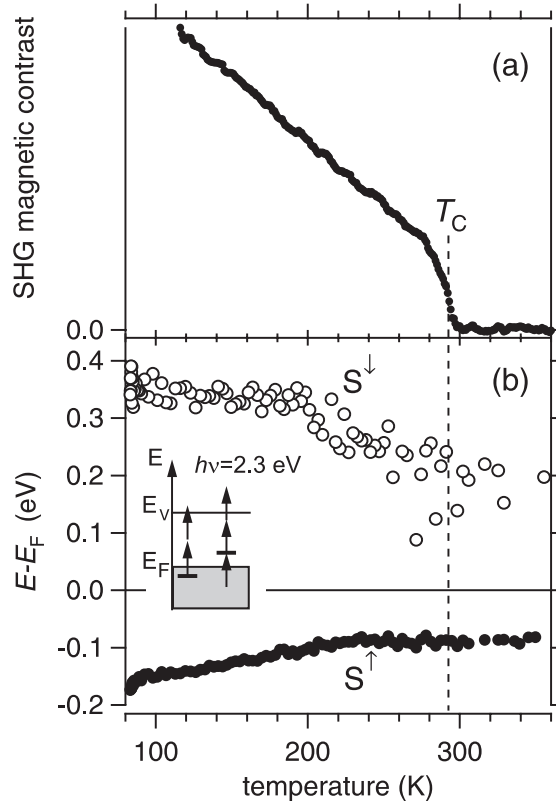
Figure 8. (a) Temperature-dependent magnetic contrast of the SHG intensity $\left(I^\uparrow - I^\downarrow\right)/\left(I^\uparrow + I^\downarrow\right)$ from Gd(0001) measured in an applied magnetic field of 500 Oe. The measurement has been carried out with increasing temperature. (b) Energy levels of the Gd(0001) surface state components $S^\uparrow$ and $S^\downarrow$ analysed by single-colour 2PPE ($h\nu = 2.3$ eV, see inset). Data have been taken while cooling. The temperature has been measured at the cryostat cold finger. At the Curie temperature the magnetic contrast vanishes, which indicates the loss of spin polarization of the $5d_{z^2}$ surface state while the exchange splitting remains at 0.3 eV.

spin-mixing contributions which account for localized spins are responsible for the loss of spin polarization, while the exchange splitting is non-zero [139, 108, 100]. As will be shown below, these results are corroborated by second harmonic generation and two-photon photoemission spectroscopy, which measure the spin polarization and the exchange splitting of the surface state, respectively.

Figure 8(a) shows the magnetic contrast of the magneto-induced SHG. This nonlinear optical method is extremely sensitive to the spin-polarization of the surface state due to its intrinsic surface sensitivity combined with resonant second harmonic generation. The resonance occurs from a generation through the unoccupied surface state component as an intermediate state in SHG as depicted in figure 7 by horizontal arrows [113]. Simultaneously, the occupied majority component acts as an initial state in SHG. The magnetic contrast, which is determined by the surface state spin polarization due to the resonant SH generation, decreases with increasing temperature quasi-linearly up to 280 K. At higher temperature, the regime of critical fluctuations near the phase transition results in a loss of the remaining spin polarization until $T_C = 293$ K is reached. No magnetic signal is observed at higher temperatures. The

lower panel of the figure shows the temperature-dependent binding energies of the exchange-split surface state which carries the spin polarization measured by the magnetic contrast in SHG. The energy levels are analysed from the temperature-dependent 2PPE spectra detected in normal emission. As shown in the inset, the occupied component $S^{\uparrow}$ is probed by two photons. The unoccupied component $S^{\downarrow}$ is populated by absorption of one photon; the excited electron is photo-emitted within the same laser pulse by absorption of two additional photons. The respective peaks in the 2PPE spectra have been fitted by two Lorentzians after normalization to the electron distribution function. This method of analysis will be detailed in section 3.2 below for time-dependent studies. The resulting temperature-dependent binding energy is given in figure 8(b). With increasing temperature both components shift towards the Fermi energy. At the Curie point, where the spin polarization of these states vanishes (top panel), the binding energy of both components remains non-zero. Albeit the scattering in the binding energy of the unoccupied component increases due to line width broadening for larger T [136], a remaining exchange splitting of in the vicinity of T_{C} of $\Delta_{ex} = 0.26(6)$ eV is clearly observed. Thereby, our results corroborate earlier investigations. Based on this characterization of the Gd surface, the non-equilibrium dynamics on the femtosecond timescale has been studied and the respective results and discussion are given in the following sections.

3.2. Relaxation dynamics of hot electron distributions

Before the spin dynamics which are driven by optically excited electrons are addressed, non-equilibrium electron dynamics which proceed on sub-picosecond timescales will be discussed. Note that spin-flip processes driven directly by light would violate dipole selection rules[4]. Understanding of the femtosecond electron dynamics is not only a prerequisite for analysis of laser-induced spin dynamics but a very active field by itself. Recently, a profound description of the decay of single-electron excitations has been developed [46]. The regime of excited electron ensembles has been pioneered by Bokor and co-workers [48]; however, it is less mature compared to the single-electron regime. It can be studied experimentally in great detail by monitoring the electron distribution function above and below the Fermi edge as a function of pump–probe delay by TRPE [101, 48].

Such experiments have been performed on 10 nm Gd(0001) films grown epitaxially on W(110). The electron distribution is measured by photoelectron spectroscopy with a dynamic range up to 10^{5} by a femtosecond probe laser pulse $h\nu_{2}$ with a photon energy larger than the work function $\Phi = E_{vac} - E_{F} = 3.6$ eV. These pulses have been generated either by quadrupling the fundamental output of the regenerative amplifier at $h\nu_{1} = 1.5$ eV, 55 fs duration, in two beta-$BaB_{2}O_{4}$ nonlinear optical crystals for subsequent SHG, resulting in $h\nu_{2} = 6.0$ eV and 90 fs pulse duration, or alternatively the frequency-doubled signal output of the VIS OPA has been employed, which offers $h\nu_{2} = 3.3$–5.4 eV and sub-50 fs pulse duration.

First, experiments with an s-polarized probe pulse are presented. This polarization of the laser field suppresses photoemission from the $5d_{z^{2}}$ surface state due to parity conservation in the photoemission process [180]. Thus the observed spectra represent bulk states. Due to a small variation of the DOS in the bulk within 0.5 eV above and below E_{F} [98], the bulk DOS is assumed to be constant and the distribution function can be analysed as a function of pump–probe delay.

Figure 9(a) shows the photoelectron yield in normal emission in a false colour representation as a function of pump–probe delay Δt and initial state energy (equation (7)). The

---

[4] For extreme optical excitation densities, which are not available in the present experiment, Zhang and Hübner found theoretically an optically induced loss of magnetization mediated by a cooperative effect of spin–orbit coupling and the laser field [185].
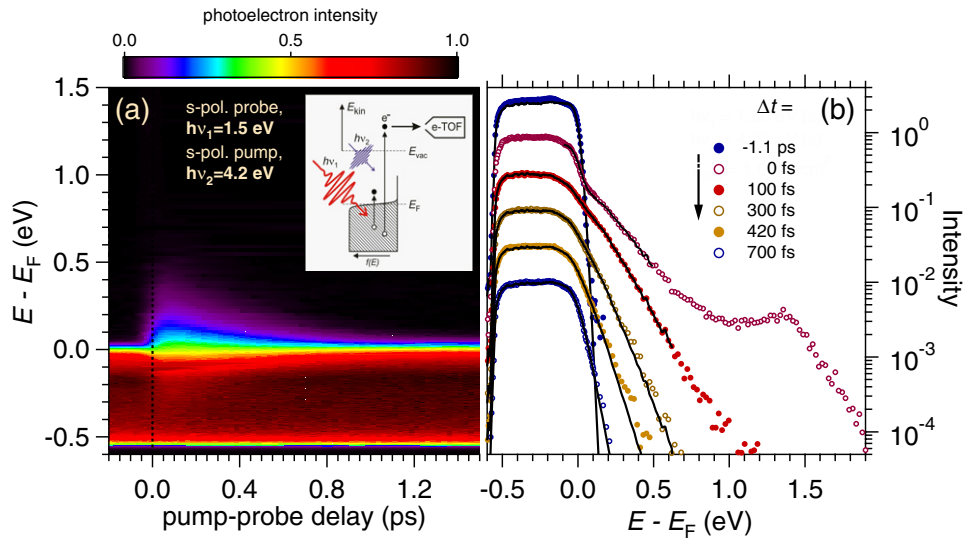
Figure 9. (a) False-colour representation of the photoelectron yield from Gd(0001) as a function of pump–probe delay and energy with respect to E_F. Pump and probe laser pulses are both s polarized. (b) TRPE spectra for different pump–probe delays. The black lines are fit functions according to a constant DOS and a Fermi–Dirac distribution function for all delays except $\Delta t = 0$ ps, where a non-thermalized distribution is required. For both panels the photoelectron yield has been normalized to unity below E_F.

absorbed IR pump fluence is 0.25 mJ cm^{-2}. PE spectra are extracted at specific delays indicated in figure 9(b). Before excitation by the pump pulse, i.e. at negative delays, the equilibrium spectrum is measured, which is shown for $\Delta t = -1.1$ ps. This spectrum, which is normalized to unity below E_F, is described by a constant DOS, a low energy cut-off determined by the probe photon energy, and the Fermi–Dirac distribution function $f(T, E) = 1/(e^{(E-E_F)/k_B T} + 1)$. The latter has been convolved with a Gaussian width of typically 45 meV to account for the band width of the laser pulse and the energy resolution of the e-TOF spectrometer. Thus, the photoelectron spectrum at negative delay determines the temperature of the sample in the laser-irradiated spot to 118 K, which is plotted in figure 10(a) for a delay of -1.1 ps. Upon excitation, a fraction of electrons in the energy interval of the pump photon energy is excited to states above the Fermi energy as illustrated in figure 1. The spectrum at 0 fs delay given in figure 9(b) is therefore strongly non-thermal and cannot be described by a Fermi–Dirac distribution. Since e–e scattering already starts to redistribute electrons within the experimental time resolution, the electron distribution increases towards E_F. However, the non-thermal character is clearly visible from the kink in the logarithmic plot near E_F at 0 fs. The peak at $E-E_F = 1.4$ eV results from a maximum in the electronic structure due to unoccupied 5d bands [43]. At 0 fs delay electrons above $E_F + 1.5$ eV are found where they cannot be excited optically. These electrons have gained energy by electron–electron scattering. After 100 fs the electron distribution has thermalized by e–e scattering and is described by a Fermi–Dirac distribution (black line, third spectrum from top in figure 9(b)), i.e. it is thermalized over the dynamic range of 10^4 given in the figure. Accordingly, an electron temperature T_e represents the electron distribution and the energy density of the excited electronic subsystem at delays later than 100 fs.

The transient electron temperature is determined by fitting a Fermi–Dirac distribution to the spectra in the vicinity of E_F and is shown in figure 10(a). Due to the non-thermal
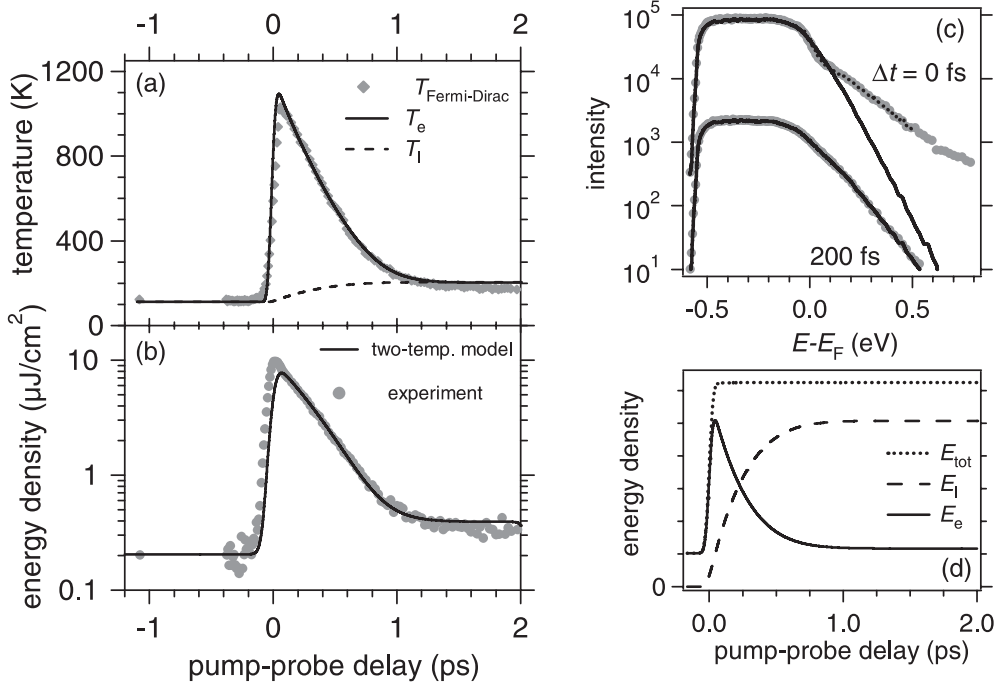
Figure 10. Time delay dependence of the temperature (a) and the energy density (b) of the electronic system. The absorbed fluence is 0.25 mJ cm^{-2}. Simulations based on the two-temperature model are plotted by solid lines (see text). (c) Exemplary TRPE spectra at 0 and 200 fs that indicate a non-thermalized and a thermalized electron distribution, respectively. Solid lines are fits according to a Fermi–Dirac distribution; the dotted line which describes the distribution at 0 fs includes two Fermi–Dirac distributions to account for a thermalized part and the non-thermal part as has been introduced in [101]. (d) Simulation from panel (b) shown on a linear scale including the lattice and electron contribution, and the total energy density after absorption of the pump laser pulse. The simulation is made for a 400 nm thick film and demonstrates the numerical stability and the energy conservation.

character of the initial distribution the temperature determined by such a fit does not describe the energy of the excited system correctly. As indicated in figure 10(c) the Fermi–Dirac fit accounts for the part of the distribution below E_F but disregards the non-thermal part, which contains most of the excess energy. Therefore, at delays -100 fs $< \Delta t < 100$ fs the electron temperatures determined by this analysis underestimate the energy of the system. At later delays, the excess energy probed by photoemission in the electron system decays by interaction with the lattice through e–ph scattering, with the spin system by e–magnon interaction, or by transport processes [101, 103], which lowers the electron temperature. The two-temperature model introduced by Anisimov *et al* [6] takes into account interaction of electrons and phonons and diffusive heat transfer processes. It is described by the coupled differential equations

$$C_e(T_e)\frac{\partial T_e}{\partial t} = S(z, t) - H(T_e, T_l) + \frac{\partial}{\partial z}\left(\kappa \frac{\partial T_e}{\partial z}\right) \tag{8}$$

$$C_l(T_l)\frac{\partial T_l}{\partial t} = H(T_e, T_l). \tag{9}$$

$C_e = \gamma T_e$ and C_l are the electron and lattice specific heat capacities; κ is the electronic part of the thermal conductivity, which is responsible for diffusive transport of energy in the

electron system. The corresponding process for the lattice is neglected because it proceeds on timescales of several hundred picoseconds, which are not discussed here. $S(z, t)$ is the source term determined by the energy density absorbed per unit time within the optical penetration depth and its dependence along the normal direction z. The electron thermal conductivity κ is taken as temperature dependent [21]: $\kappa(T_e) = \kappa_0 T_e/T_l$. The e–ph coupling is modelled with an energy-transfer rate $H(T_e, T_l)$ that was derived by Kaganov *et al* [87] by summation of all one-phonon emission and absorption processes assuming thermal electron and phonon distributions. The temperature dependence of C_l is described using the Debye approximation with a high temperature value of $C_l(T \rightarrow \infty) = 40$ J mol^{-1} K^{-1} [38]. Using literature values of $\kappa_0 = 11$ W m^{-1} K^{-1} [82], $\gamma = 225$ J m^{-3} K^{-2} [75], the optical penetration depth of 40 nm [169] (also see footnote 2), and the Debye temperature of 163 K [161], the measured transient electron temperature is reproduced (figure 10(a)). Following Hohlfeld *et al*, ballistic electron transport is included through an effective increase of the penetration depth by 20 nm [79]. Small deviations near time zero are attributed to the presence of the non-thermal electrons. The relaxation in T_e and the observed equilibrium temperature of 200 K at $\Delta t = 2$ ps is well reproduced.

The energy density is a property that is well defined at all time delays unlike the electron temperature which requires a thermalized electron distribution. The energy density takes into account thermal and non-thermal electron distributions by integrating the TRPE spectrum at each delay over energy:

$$\varepsilon_e(t) = 2 \int_{E_F=0}^{2\text{ eV}} N(E, t)|E|\, dE. \tag{10}$$

The energy of excited holes is taken into account by the factor of two. This is based on earlier work on Ru(0001) [101], where it was shown that electrons and holes contain identical excess energy. The transient energy density normalized to the density of states within the top 5 Å per eV and per atom is shown on a logarithmic scale in figure 10(b). The electron attenuation length is taken as the photoelectron escape depth [125]. The equilibrium value 0.2 μJ cm^{-2} at negative delays before the excitation is increased by a factor of 48 due to absorption of the laser pulse. Subsequently, the energy density relaxes to a value that describes the equilibrium between electrons and the lattice. The transient energy density has been simulated by converting the electron temperatures obtained by the two-temperature model to energy using the electron heat capacity: $\varepsilon(t) = C_e(t)T_e(t)/2 = \gamma T_e^2(t)/2$. Figure 10(b) indicates that the measured $\varepsilon(t)$ is well described for delays longer than 100 fs. In figure 10(d) the total deposited energy is shown together with the energy in the electron and the lattice system. At delays < 100 fs, a non-thermal heat bath has to be taken into account as an additional contribution to ε [101] that might be responsible for the rise of the excess energy within the laser pulse duration, which is slightly faster than determined by the simulation in figure 10. Moreover, the maximum value of the experimentally determined $\varepsilon(t)$ which is 23% higher in the experimental data compared to the simulation might be related to the non-thermal heat bath. To improve further the description of the experimental data, the film thickness and reflection of ballistic electrons at the Gd/W interface needs to be implemented in an extended heat bath simulation which is currently underway. Furthermore, the simulation according to the 2TM does not take into account the magnon system explicitly. Magnons are well known to contribute to the heat capacity because it presents a pronounced peak at the Curie temperature [38]. Thus the present description is to be considered as an effective model where the energy transfer from the electron system to the phonon and magnon system is described by a single, effective scattering rate $\Gamma_{e-ph/m}$ accounting for e–ph and e–magnon scattering (see also section 3.3).

It is worth noting that during delays where a non-thermal distribution is encountered the distribution function can be described surprisingly well by the sum of two Fermi–Dirac distributions with different temperatures as depicted in figure 10(c) by the dotted line. As discussed in detail in [101], the colder distribution represents the thermalized part while the non-thermal part is described by the second 'auxiliary' distribution. A theoretical result that corroborates our experimental study has been obtained by Rethfeld *et al* [138]. These authors use a kinetic description and calculate Boltzmann collision integrals explicitly without phenomenological parameters and find a behaviour very similar to our experimental observation: before the electron distribution is fully thermalized, e–e scattering among excited electrons contributes significantly, which corroborates the existence of the non-thermal distribution. This is also evident from the analysis of the transient line width of the $S^{\uparrow}$ component in section 3.3. Furthermore, Rethfeld *et al* point out that for a high excitation limit near the damage threshold the energy exchange between electrons and lattice can be described with the two-temperature model, despite the non-equilibrium distribution function of the electron gas. At lower excitation density it is found that the non-equilibrium distribution leads to a cooling of the electron gas delayed compared to the two-temperature model. This is not observed in figure 10(b), which is in agreement with an estimated excited electron density of about 10% of the electrons available near E_{F} obtained by the ratio of electrons in the thermalized and the non-thermalized distribution at $\Delta t = 0$ fs. We exclude laser damage since all experimental data are averaged over several scans of the time delay and are well reproducible.

For the discussions below it will be important to understand the origin of a pump-induced variation of a specific spectroscopic signature. It is a consequence of the above analysis that a change in the energy transient during the thermalization of the electron subsystem which is close to the duration of the laser pulse is of electronic origin or is mediated by hot electrons. In contrast, a feature that presents a change from its equilibrium value to an intermediate state with a slower characteristic time of e.g. ∼0.5 ps, when the electron system has thermalized, represents energy transfer to phonons or magnons (see figures 10(b), (d)).

By changing the polarization of the probe laser pulse to p polarized, the surface state is probed in addition to bulk states because the p-polarized optical field conserves the wavefunction parity in the excitation process [180]. Figure 11(a) shows the photoelectron yield at 100 K equilibrium temperature as a function of initial state energy and pump–probe delay. For all delays a pronounced peak is observed at about 0.18 eV below E_{F}, which originates from the occupied component $S^{\uparrow}$ of the surface state. From the false-colour plot several transient effects can be recognized: (i) a weak, albeit well resolved, transient shift of the binding energy, (ii) a reduction off the peak intensity in $S^{\uparrow}$ near time zero, which recovers gradually, albeit not completely, until 2 ps, and (iii) hot electrons above the Fermi level. In the representation of the corresponding TRPE spectra shown in figure 11(b) on a logarithmic intensity axis the hot electrons are recognized more clearly. A shoulder on top of the electron distribution function which was not present for s-polarized probe pulses is clearly identified. Its energy 0.4 eV above E_{F} agrees with binding energies of the unoccupied surface state component $S^{\downarrow}$, which has been discussed in figures 7 and 8(b).

However, before we address these pump-induced changes in the PE spectra the transient energy of data generated with s- and p-polarized probe pulses are compared in order to estimate the surface and bulk excitation efficiencies. The energy density which is obtained from the TRPE spectra representing surface and bulk states is determined according to equation (10). In figure 12 it is compared to dynamics in the bulk. Both energy transients are measured under comparable conditions at an absorbed fluence of 1.2 mJ cm^{-2} for s- and p-polarized probe pulses, respectively. Overall, very similar excitation and relaxation dynamics are encountered.
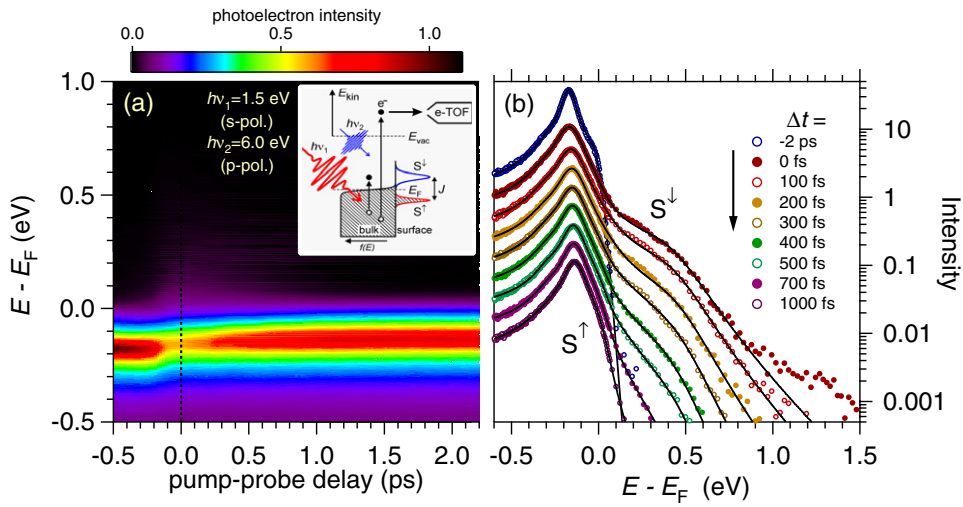
Figure 11. (a) False-colour representation of the photoelectron yield from Gd(0001) as a function of pump–probe delay and energy with respect to E_F. While the pump laser pulse is s polarized, the probe pulse is p polarized to monitor the occupied $S^\uparrow$ and unoccupied $S^\downarrow$ surface state components. (b) TRPE spectra for different pump–probe delays. The lines are fit functions according to a constant DOS from bulk, two Lorentzians that account for the surface state components, and a non-equilibrium distribution function. See [103].
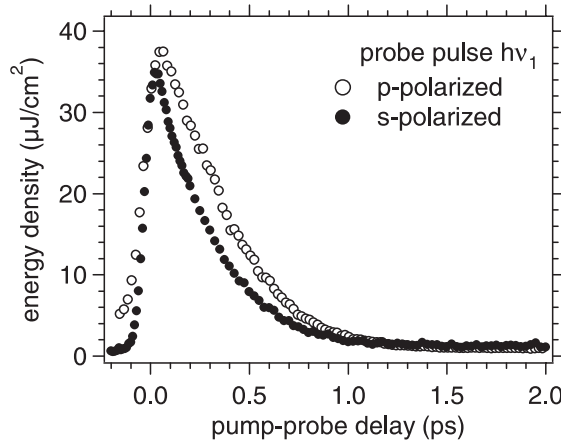

Figure 12. Comparison of the transient energy density measured under comparable conditions with s- and p-polarized probe laser pulses at an absorbed pump fluence of 1.2 mJ cm^{-2} and an equilibrium sample temperature of 100 K. The escape length of photoelectrons is about 5 Å [125].

The maximum energy density of the p-polarized data which monitor the bulk and the surface state is about 2 μJ cm^{-2} larger than the maximum $\varepsilon(t)$ for the bulk sensitive probe (s-pol.). This is reasonable because electrons are photoemitted from the few topmost Gd layers within $\sim$5 Å escape depth [125] and the photoelectron yield from the surface state in the case of p-polarized probe pulses adds on top of the photoelectron yield generated with s-polarized light. The decay of the energy density appears to be slightly delayed in the case of the p-polarized probe compared to the s-polarized one, while the equilibrium values at 2 ps coincide. This suggests a slightly weaker e–ph (or e–magnon) interaction at the surface compared to bulk,

which can, in principle, be conceived by different spatial distributions of the corresponding electronic wavefunctions. However, this first indication of a different relaxation for surface and bulk is subject to further investigation.

3.3. Time evolution of the self-energy of the $5d_{z^2}$ surface state

The aforementioned transient changes in the PE spectra give detailed insight into the elementary processes on ultrafast timescales. From figure 11 variations in the PE intensity are well discernable, which suggest—assuming constant photoemission matrix elements—pump-induced changes in the electron population due to electron–hole pair excitation. In addition, the binding energy and the line width, i.e. the real and the complex part of the self-energy, respectively, present clearly resolved pump-induced changes. The complex self-energy has been introduced to account for interactions among elementary excitations of the various degrees of freedom in solid matter like electron–hole pairs, phonons, and magnons [46, 106]. Thus, its measurement facilitates in general access to these scattering events. The imaginary part defines the scattering rate measured in PE spectroscopy under equilibrium conditions by the line width Γ [122, 137]. Separation of the e–e, e–ph, and e–impurity scattering has been obtained [137, 164] for surface states on metal surfaces. This analysis is based on the quasi-linear temperature dependence of Γ, which is determined by the e–ph interaction and allows determination of the mass enhancement parameter λ. In the case of the $5d_{z^2}$ surface state on ferromagnetic Gd(0001) this analysis of temperature-dependent data includes e–magnon scattering [52, 173].

Pump-induced changes under the excitation densities employed in the present study, where the ensemble of conduction electrons is driven out of equilibrium [101, 48, 103], facilitate an investigation of the time evolution of occupied electronic states and the respective self-energy [141]. Note that this is a different regime compared to lifetime studies of individual holes measured by the line width in PE spectroscopy or single-electron excitations and the scattering events responsible for their relaxation investigated in time-resolved 2PPE [174, 129, 55, 117]. In the present study, a considerable fraction of the conduction electrons is excited, which results in changes of the distribution function as discussed above in section 3.2. An alternative approach to e–ph coupling employs angle-resolved photoemission spectroscopy. Due to electron–phonon coupling the spectral function near the Fermi wavevector reveals a well defined quasiparticle peak. The coupling constant λ is estimated from the respective renormalization of the quasi-free electron mass [74, 155].

In the following we analyse the TRPE spectra of figure 11 by a fitting procedure and determine the temporal evolution in binding energy, line width, intensity of the occupied surface state component, and exchange splitting of both surface state components as a function of pump–probe delay. We separate the surface spectral function from the distribution function $f(E, \Delta t)$ and bulk contributions as illustrated by figure 13, which depicts an exemplary spectrum at a delay of $\Delta t = 300$ fs. To fit the spectrum, two Lorentzians for $S^{\uparrow,\downarrow}$, a constant bulk density of states, and a non-equilibrium distribution function $f(E, \Delta t)$ are considered. As shown in [140, 59], unoccupied states can be analysed with photoemission by normalizing the spectrum with a Fermi–Dirac distribution. On femtosecond timescales non-thermalized electrons contribute significantly to the spectrum as has been discussed in section 3.2 and the literature [101, 48]. This introduces corrections of the Fermi distribution which become apparent on a logarithmic scale (figure 10(c), figure 13). In the case of the well resolved spectra taken with a p-polarized probe pulse, optimum fitting requires inclusion of the non-equilibrium part of the distribution function up to a delay of 300 fs, as is recognized from the weak kink in the distribution function 50 meV above $E_{\rm F}$ (figure 13, dashed line). After determining the
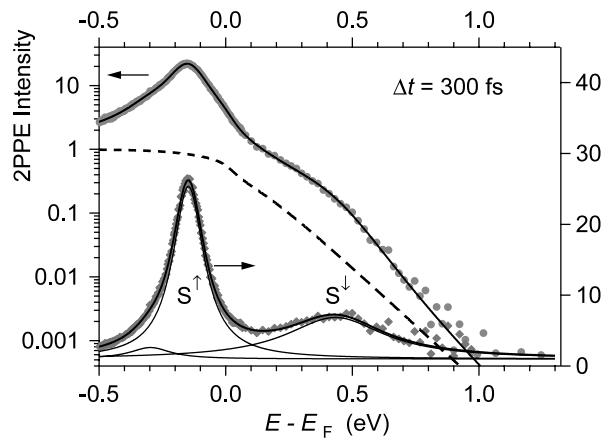
Figure 13. Separation of a TRPE spectrum into the distribution function (dashed line, with respect to the left axis) and the surface state components (with respect to the right). The fit of the TRPE spectrum, shown here for 300 fs as an example, consists of (i) the non-equilibrium distribution function which requires to be a combination of a thermalized and non-thermalized distribution to fit the spectrum close to E_F, (ii) two Lorentzians for the surface state components, (iii) a third weak Lorentzian, which has been reported in ref. [136], and (iv) a convolution with a Gaussian of typically 45 meV width to account for the experimental resolution. Dividing the spectrum by the distribution function results in the spectral density of the surface depicted by grey diamond symbols. See also [103].

fit function to the spectrum (figure 13, topmost solid line) the surface contribution $S^\uparrow$ and $S^\downarrow$ becomes well discernible by normalizing the spectrum to the non-equilibrium distribution function. Neglecting the non-thermal part in $f(E, \Delta t)$ lowers the quality of the fit close to E_F. On the other hand, it needs to be pointed out that none of the results discussed below depend on including non-thermal electrons and present robust effects. Non-thermal electrons are included in the analysis because otherwise the fit would be of lower quality and error bars on the fit parameters would increase.

The right panel of figure 14 shows the transient population which is derived from the PE intensity of the $S^\uparrow$ component. The population is normalized to the equilibrium value at 100 K taken from negative delays and is determined by integrating over the PE line up to E_F. Upon laser excitation the population decreases by 22%, which means that the pump laser pulse excites every fifth electron in $S^\uparrow$ to unoccupied states. Relaxation of this depletion occurs within the first picosecond, that means by cooling of the hot electron distribution driven by interaction of electrons with other quasiparticle excitations. At delays later than 1 ps, the population decreases on a second, slower timescale, which occurs due to a transient shift of the binding energy towards the Fermi level over several picoseconds.

3.3.1. Transient line width variations. The left panel of figure 14 depicts the line width of the occupied surface state component as a function of pump–probe delay. The analysis of the experimental data takes into account an experimental broadening of 45 meV stemming from the bandwidth of the femtosecond laser pulse and the energy resolution of the electron spectrometer. For determination of the transient line width the experimental broadening is considered as constant. As a result we find that the equilibrium line width of the occupied surface state component at 90 K is 53 meV, which increases more than threefold within the laser pulse duration and relaxes to 130 meV after 2 ps (figure 14).
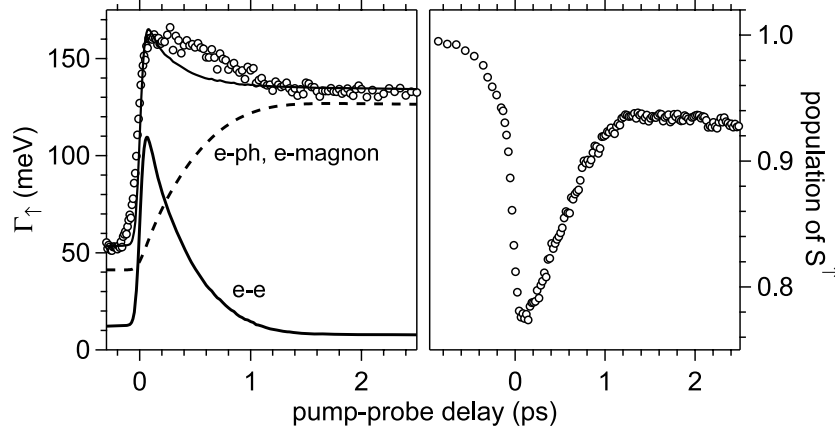
Figure 14. Left: experimentally determined transient line width of the $S^{\uparrow}$ surface state component, which increases threefold upon absorption of the pump laser pulse. The behaviour has been analysed by a model based on the two-temperature model with line width contributions from e–e and e–ph scattering. Right: transient population of the occupied surface state normalized to the equilibrium value at 90 K, which quantifies the optical excitation. See [103, 105].

The line width of electronic states is described by the spectral function $A(E, \mathbf{k})$ determined by the self-energy of the photo-hole $\Sigma(E, \mathbf{k})$, which consists of contributions from quasiparticle interaction like e–e, e–ph, e–magnon, and e–defect scattering [81, 46]. The inverse electronic lifetime is given by $\Gamma = 2 \, \text{Im}(\Sigma)$. Following Matthiessen's rule the scattering rates of the different processes add up to the total rate Γ.

$$\Gamma(E, T) = \Gamma_{\text{e–ph/m}}(E, T) + \Gamma_{\text{e–e}}(E). \tag{11}$$

Under equilibrium conditions a linear increase in the line width with temperature is observed [52, 136, 111, 110]. This result has been analysed by a theoretical description of the e–ph contribution to the line width according to the Eliashberg e–ph coupling function $\alpha^2 F(\omega)$ and the respective Fermi–Dirac and Bose distribution functions [60, 110]. For temperatures $T > \Theta_D/3$, Θ_D is the Debye temperature, a linear temperature dependence is found. The effective scattering rate $\Gamma_{\text{e–ph/m}}$ introduced in equation (11) accounts for e–ph and e–magnon scattering that both transfer energy from the electron subsystem to other degrees of freedom of the solid. To include e–magnon scattering explicitly, one could consider a three-temperature model including a spin temperature as suggested in [12] and a separate scattering rate $\Gamma_{\text{e–m}}$. Out of two reasons we use the simpler approach of an effective $\Gamma_{\text{e–ph/m}}$.

(i) The e–magnon scattering probability under the employed non-equilibrium condition is not well understood and the author is not aware of an applicable model description like the Eliashberg coupling function is for e–ph scattering.

(ii) Focusing on the strong line width changes upon the optical excitation, a first goal is to describe the evolution of the e–e scattering probability and the energy transfer from the electron subsystem into other subsystems.

We assume in the following that also the effective $\Gamma_{\text{e–ph/m}}$ varies linearly with the lattice temperature, which is reasonable since both scattering partners are bosons. We cannot account for differences in the scattering matrix elements but follow earlier experimental and theoretical findings that the strengths of e–ph and e–magnon interaction are for Gd of the same order of magnitude [54, 152, 149, 73].

$$\Gamma_{\text{e–ph/m}}(E, T_l) \approx 2\pi \lambda k_B T_l. \tag{12}$$

Here λ represents the e–ph mass-enhancement factor and T_l the temperature of the lattice. To account for the e–e contribution to Γ the Fermi-liquid description is considered as a first approximation. Then, the electron lifetime is determined by the phase space available for e–e scattering and $\Gamma_{e-e} = \beta(E_i - E_F)^2$. The broadening of the Fermi–Dirac distribution with electron temperature leads to a term that increases $\propto T_e^2$ [130, 111]:

$$\Gamma_{e-e} = \beta[(\pi k_B T_e)^2 + (E_i - E_F)^2]. \tag{13}$$

The proportionality constant β describes the probability of e–e collisions and accounts for screening of the Coulomb interaction. Note that in thermal equilibrium $T_e = T_l$. Under the severe non-equilibrium of the electron and phonon distributions, which prevails during the first picosecond after absorption of the laser pulse, different transient temperatures $T_e > T_l$ are required to describe the Fermi–Dirac and the Bose distribution functions in equations (13) and (12), respectively. As recognized from the top solid line in figure 14 (left), the experimental transient line width of the $S^\uparrow$ surface state component can be well fitted by combining equations (11), (12), and (13). The lattice and electron temperatures T_l, T_e are taken from the corresponding 2TM simulation (cf figure 10(a)), the binding energy E_i of $S^\uparrow$ is determined as described above (figure 13), and $\beta = 0.2$ eV^{-1} and $\lambda = 0.95$ are fit parameters constrained close to literature values from [52, 136]. Figure 14 shows the fit to be in good agreement with the experimental data and depicts in addition the e–e and e–ph/m contribution to the transient evolution of Γ.

Thereby we could show that during the optical excitation and the following several hundred femtoseconds the line width increase is dominated by e–e scattering of hot carriers among each other, which decays to an equilibrium level within 1–2 ps, i.e. on a timescale identical to the relaxation of the energy density in the electronic subsystem (figure 12). $\Gamma_{e-ph/m}$ increases due to a rise in the lattice temperature and is the dominating contribution to the measured line width after about 500 fs, where Γ_{e-e} has decreased. Thus, the combination of both line width contributions is responsible for (i) quasi-instantaneous increase in Γ and the remaining large line width after several picoseconds. In contrast to earlier work in equilibrium [52, 136, 111, 110], our finding demonstrates a dominant contribution to Γ due to electron–electron scattering which is proportional to T_e^2. This was possible only by generating a non-equilibrium condition among electrons, phonons, and spin excitations.

This analysis of the transient line width contains approximations which are addressed in the following.

(i) Due to the extensive analysis of the elementary processes responsible for the decay of electronic excitations at metal surfaces during the last decade [46], it is by now well established that the Fermi-liquid picture is in general an oversimplification. The decay of hot electrons proceeds through inter- and intraband scattering with probabilities which depend on the electronic structure of the specific surface and underlying bulk. Only in a situation where the excitation in the surface state decays exclusively through bulk states with a fairly constant electronic DOS might this approximation be justified. The very similar transient energy densities for electron dynamics probed with s-polarized and p-polarized laser pulses (figure 12) favour such a scenario.

(ii) Scattering of valence electrons under magnon emission (or absorption) facilitated by e–magnon interaction represents a well established relaxation mechanism of excited electrons or holes [64, 54, 152, 149, 73]. In principle, it could be taken into account explicitly in the above analysis e.g. by considering the interaction parameters derived by Allen [5]. At the current stage electron–magnon scattering is considered implicitly by the electron mass enhancement factor λ which has been determined to be $\lambda = 1.0 \pm 0.3$ in a temperature-dependent scanning-tunnelling spectroscopy study [136]. Since this experiment averages both spin directions, the

temperature-dependent line width increase comprises e–magnon and e–ph contributions and gives an effective parameter. A detailed look at figure 14, left, shows that at delays between 0.2 and 1 ps the line width is not well described by the simulation using the two-temperature model. Supposing that e–magnon scattering would proceed on a slightly faster timescale than e–ph interaction, such a hump in the transient line width could be generated, which is subject to further investigation.

(iii) Defect-induced scattering is known to generate dephasing of the excited electron wavepacket by elastic scattering events [128], which has been investigated systematically for adatoms on noble metal surfaces by Fauster and co-workers [20]. In equilibrium, defect-induced scattering generates a broadening of the line [137]. Such processes have not yet been taken into account in the above analysis of the transient line width. However, a comparison between the equilibrium line width of the present study with literature shows a notable variation. While in the present work a line width of 52 meV at 90 K (see figure 14) and 28 meV at 30 K (see [105]) is reported for optimized annealing conditions, 80 meV at 90 K (and 40 meV at 12 K) have been observed by Bauer and co-workers using STS on several 100 Å wide Gd islands or terraces [136]. Fedorov *et al* determined the line width of the occupied majority component by spin-resolved PE spectroscopy to be another 10–20 meV broader [52]. Albeit the effect of defect-induced scattering might be smaller in the case of the strongly localized d_{z^2} Gd(0001) surface state compared to noble metal surfaces, such variations in line width ask for a more detailed investigation and a clarification of defect-induced contributions [137].

3.3.2. Transient variations in binding energy. The above analysis of the time-dependent line width with identification of time intervals with dominating e–e and e–ph/m scattering serves as a characterization of the optically excited state. This understanding is helpful for an analysis of pump-induced changes observed in the binding energy of the occupied component of the $5d_{z^2}$ surface state, which is discussed in the following.

A fluence dependence of the pump-induced variation of the binding energy has been recorded at an equilibrium temperature of 30 K to investigate the impact of excitation density on the binding energy[5]. Figure 15 shows the temporal evolution of the energy level of the occupied surface state component with respect to E_F for absorbed pump fluences between 0.02 and 1.32 mJ cm^{-2}. Obviously, the pump-induced effects strongly depend on fluence. With increasing F we find that the behaviour changes from an initial stabilization of the occupied surface state component to a shift towards E_F at $\Delta t = 2$ ps. In more detail, the binding energy change upon laser excitation during the first 0.5 ps, where the excess energy resides in the electron subsystem (figures 10, 14), first evolves and then changes its sign with increasing F. At delays of 2 ps, after electrons and phonons have equilibrated, the energy level shifts for all fluences closer to E_F and the energy shift increases with F. Apparently, these opposite trends at early and later delays compete with each other. For the maximum fluence we observe exclusively a continuous energy shift towards E_F without the complication of a stabilization during the first 0.5 ps. This excitation condition characterizes the regime where the destabilization of the occupied surface state component (shift of the energy level towards E_F) dominates over the stabilization (shift towards the valence band bottom).

This limit (max. F) is discussed in the following. We exclude that this continuous shift in binding energy is generated directly by optically excited electrons because the energy shift builds up while the excess energy density in the electronic subsystem ε_e decays already (figures 10, 12). Thus, this destabilization occurs due to either hot phonons or magnons and

---

[5] As reported in [105], the transient evolution in the line width shows a very similar behaviour compared to 90 K equilibrium as shown in the present paper, and the above conclusions of e–e and e–ph/m scattering dynamics also hold for an equilibrium temperature of 30 K.
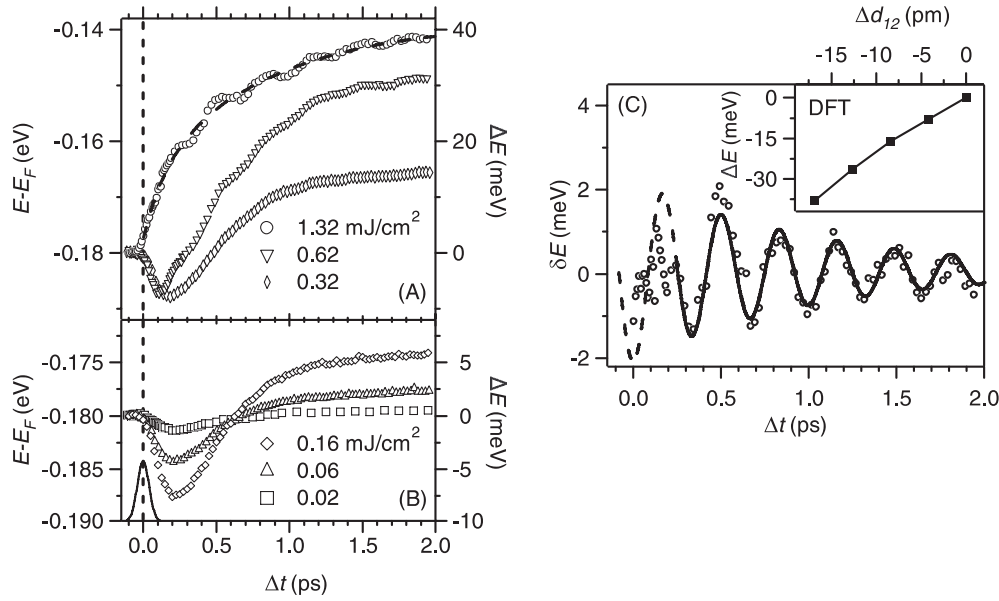
Figure 15. Time evolution of the energy level of the occupied surface state component at an equilibrium temperature of 30 K for high (A) and low (B) absorbed fluences, as indicated. The temporal resolution is given by the lower solid line in (B), representing the two-photon photoemission intensity from occupied electronic states. Variations in the equilibrium binding energy for subsequent film preparations are of the order of 10 meV and the equilibrium energies have been aligned at $E - E_F = -180$ meV. (C) The oscillatory component of E_B extracted from the $F = 1.32$ mJ cm^{-2} data by subtraction of the incoherent contribution (dashed line in panel (A)). The solid line represents a fit to the oscillatory component using an exponentially damped cosine; the dashed line shows its extrapolation to time zero. Inset: increase in the binding energy upon contraction of the spacing d_{12} between the surface and the subsurface layer calculated by Bihlmayer *et al* using density functional theory [98]. See [105].

represents an incoherent thermal response of the surface. Anticipating the result of a constant exchange splitting of the surface state components with pump–probe delay, which signifies the absence of binding energy variations due to magnetic excitations (see section 3.4), we conclude that the destabilization arises from heating effects like thermal expansion.

Now we turn to the stabilization observed for smaller F at earlier delays. The largest shift towards the valence band bottom, i.e. the most strongly bound configuration, is found at $\Delta t \approx 200$ fs, i.e. while the excess energy resides in the electron gas. Considering the electronic structure of the Gd(0001) surface, depicted for the $\overline{\Gamma}$ point in figure 7, the intense optical excitation redistributes electrons among surface and bulk states. Majority electrons are excited by the 1.5 eV pump photons from the occupied surface state component to unoccupied majority bulk states. Minority bulk electrons are lifted into the unoccupied surface state component. In addition to these direct excitation channels at the surface, bulk–bulk transitions occur further out in the Brillouin zone, see [98] for the Gd valence band structure, and will excite the surface indirectly through electron–electron scattering processes. Supposing that the pump-induced stabilization would represent a purely electronic effect, it is to be expected that its build-up follows the energy density of ε_e and thus the laser pulse. However, the initial shift in the energy level is clearly delayed with respect to the excitation because the laser pulse is over before the maximum stabilization has been established (figure 15). Therefore, we discard a purely electronic effect and consider a combination of the excited electronic structure and the lattice.

The optical excitation populates an excited state potential surface where the minimum occurs at some different nuclear coordinate. Since the ions require a finite time to evolve along the excited state potential surface, this effect can well account for the observation. We conclude that due to the optical excitation that redistributes electron density at the surface, the surface ions find a new, transient position.

This finding is related to the work of Petek *et al*, who reported nuclear wavepacket motion of individual Cs atoms adsorbed on Cu(111) [129]. The Cs adsorption induces occupied and unoccupied resonances with bonding and anti-bonding character, respectively. Femtosecond laser-induced population of the anti-bonding resonance weakens the Cs–Cu bond, which leads to an adjustment to the Cs–Cu distance to the non-equilibrium state and changes the electronic energy of the anti-bonding resonance. This correlation of nuclear motion and transient binding energy variation has been demonstrated in [129] by a time-resolved two photon photoemission experiment. In respect of binding energy variation upon nuclear motion, the present work represents a similar process, since the electronic structure of the Gd(0001) surface is excited resonantly (figure 7) and the surface ions react accordingly. The difference is that in the Gd(0001) case occupied electronic states are analysed, i.e. the holes generated by the optical excitation (and the hole-driven nuclear dynamics) rather than the excited electrons as in the case of Cs/Cu(111).

A closer look at the high fluence data in figure 15 reveals in addition to the aforementioned stabilization and destabilization effects a periodic contribution in the binding energy evolution. It is separated from the background by subtraction of the incoherent, thermal contribution (dashed line, figure 15(A)) and the oscillatory component δE is given in figure 15(C). After 250 fs we resolve a damped oscillating behaviour with a frequency of 3.0(1) THz and a damping time of 1.0(1) ps as determined by a fit to the data (solid line). At delays < 200 fs the steep background inhibits the analysis of the oscillatory contribution and the fit is extrapolated to time zero (dashed line). The oscillation amplitude is 2 meV, small but clearly resolved because of the sharp spectroscopic feature of the occupied surface state component, which facilitates the analysis of such small pump-induced variations in binding energy. Since the phase of this excitation is well defined with respect to the optical excitation at time zero we refer to this excitation as a coherent mode following the terminology of optically excited coherent phonons [39]. The observed frequency is close to that of the LO phonon at $q = 0$ in Gd bulk at 3.18 THz [135], where the basal planes of hcp Gd vibrate with respect to each other and the optical magnon mode at 3.5 THz and $q = 0$. At the surface the LO derived mode represents a vibration of the surface layer with respect to the underlying bulk, modulating d_{12}. The phonon and magnon contribution of this coherent excitation is investigated by nonlinear optical pump–probe experiments; see section 4.

Here we continue with a quantitative analysis of the periodic binding energy changes. For this purpose density functional (DFT) calculations using the general gradient approximation have been carried out by Blügel and co-workers [105, 98]. It is observed that for a change of d_{12} the surface state's binding energy varies. Upon a contraction of the interlayer distance the surface state is stabilized (inset in figure 15(C)). This behaviour is found for the occupied and the unoccupied (not shown) component of the state [18]. A change in exchange splitting upon reduction of d_{12} has not been found albeit the magnetic moment of the 4f electrons is included in the calculation. Therefore, we conclude that the phonon dynamics are responsible for the periodic variations observed in the binding energy. Since the surface phonon mode modulates d_{12}, DFT calculations of the surface state energy changes upon a contraction d_{12} offer in combination with the dynamic binding energy variations an estimate of the coherent phonon amplitude in real space. Based on the quasi-linear variation of the energy level of the occupied surface state component with d_{12} (figure 15(C) inset) we estimate from the amplitude

$\delta E_0 = 2$ meV the initial, coherent lattice displacement to be about 1 pm or $3 \times 10^{-3} d_{12}$. This is a small, but reasonable phonon amplitude for the employed excitation conditions. The present case is a first example to investigate the modification of electronic structure upon interaction with a phonon. A closely related example has recently been published for the insulating phase of TaS_2, where the presence of a charge density wave increases electron–phonon coupling and the modulation of the equilibrium binding energy is up to 20 meV [126].

Finally, we compare time regimes where the excess energy resides in the electronic subsystem for low and high F. The maximum in δE_B, extrapolated to $\Delta t = 0$, defines the phase of the oscillations (figure 15(C)). Thus, the time delay of the maximum in δE_B is clearly different compared to the low fluence regime where the maximum change in E_B occurs delayed at 200 fs when δE_B for large F is smallest (figure 15). This fact corroborates the excitation mechanism of the coherent phonon. Photon absorption populates an electronically excited potential surface. In this potential, which is determined by the electron ensemble and is displaced with respect to the ground state, the surface ions oscillate with a cosine-like phase. Our study shows that the lattice vibration can only be launched if an excited state of the electron ensemble is populated (figure 3), which is not the case for lower F. The ions move nevertheless, but the lattice dynamics proceed in the ground state potential and the change in lattice displacement evolves gradually rather than instantaneously as for the high F regime.

3.4. Spin-mixing and electron–magnon scattering on a femtosecond timescale

Since Gd is a ferromagnetic metal magnetic excitations present a considerable contribution to the specific heat of the material [38]. Magnon excitation, either driven directly by optically excited electrons or indirectly by phonons which have been excited by hot electrons, has to be included in a complete description of ultrafast dynamics in solid matter. This section investigates pump–probe experiments on spin dynamics in ferromagnets on femtosecond timescales and addresses elementary excitations of the ordered spin system directly in the time domain. Up to now, similar investigations have focused on 3d ferromagnets using magneto-optical methods [12, 78, 96, 62, 16], photoemission [140, 144], and theory [185]. Basically, all these studies conclude that after optical excitation ultrafast demagnetization occurs within several hundred femtoseconds. Various mechanisms based on spin–orbit, electron–spin, and phonon–spin interaction have been discussed in review articles [184, 94], but the responsible elementary processes have not been clarified. We aim at the elementary spin-dependent processes on a femtosecond timescale which are responsible for ultrafast changes of the spin polarization of the Gd(0001) surface, which then can be considered for other systems as well.

The present study combines the complementary experimental methods of TRPE, which is a powerful tool to study the electron and phonon relaxation dynamics of optically excited systems and time-resolved nonlinear magneto-optics using SHG from the Gd(0001) surface. The optically excited state and its relaxation dynamics has been analysed above and we proceed with the magneto-optical data to investigate spin-dependent processes.

The time-resolved nonlinear magneto-optical field $E_{odd}^{2\nu}$ displayed in figure 16 represents a drop to 50% of the equilibrium value within the pulse duration. The pronounced oscillations with a period of 340 fs originate from a coherent phonon–magnon mode at the surface, which is addressed in section 4. A similar behaviour is found for lower optical excitation density. Since the coherent dynamics will be covered in the coming section, the incoherent part determined by subtraction of the oscillatory component is displayed here by lines for different pump fluences. A filtering procedure [114] gives the non-oscillatory part depicted in figure 16. We find that the initial drop in $E_{odd}^{2\nu}$ increases linearly with pump fluence, which asks for an ultrafast loss
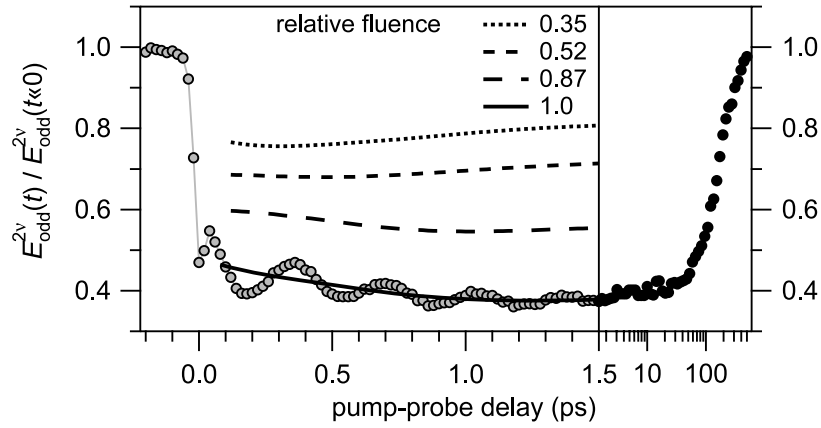
Figure 16. Time-dependent odd SH field representing the spin polarization of the Gd(0001) surface state. Lines depict the incoherent contribution for different relative pump fluences (maximum absorbed fluence ≈ 1 mJ cm^{-2}) after subtraction of the oscillatory part which originates from a coherent phonon–magnon mode; see section 4. Reprinted with permission from [103]. Copyright 2003 American Physical Society.

mechanism of spin polarization mediated by optically excited electrons. Artefacts in magneto-optics due to dichroic bleaching have been discussed for 3d ferromagnets [96, 62, 121]. They are of minor importance in the present case because no significant variation of the magneto-optical signal that evolves in parallel with the energy relaxation in the electronic subsystem is observed. Furthermore, the drop in $E_{\mathrm{odd}}^{2\nu}$ remains up to 40 ps. Recovery of the magneto-optical signal (right panel of figure 16) occurs on a 100 ps timescale, which indicates that this rather slow relaxation originates from lattice cooling, which is mediated to the spin systems by spin–lattice interaction [166]. It clearly differs from the relaxation of optically excited electrons, which occurs within the first picosecond after excitation (figure 12).

The exchange-split electronic structure of the Gd(0001) surface facilitates a direct comparison of the evolution of a magneto-optical signal representing the spin-polarization and of the exchange splitting itself. The latter has been achieved by TRPE. The respective experimental data have been shown in figure 11 and the procedure to separate the distribution function and the spectral function of the surface state has been introduced (figure 13). Following this data analysis the spectral function of the Gd(0001) surface has been determined for different delays and is given in the right panel of figure 17. The resulting transient variation of the binding energies of both surface state components with respect to E_{F} are shown on the left in figure 17. The time-dependent energy levels of the occupied and the unoccupied component are shown in the left panel. The dependence of the occupied state has been discussed in the preceding part. However, the energy of the unoccupied $S^{\downarrow}$ has not yet been addressed. Analysis of such small changes as for the occupied component is hindered for $E(S^{\downarrow})$ due to its larger line width and the lower intensity, which leads to error bars larger than the shift of $E(S^{\uparrow})$. Nevertheless, it is clear that the exchange splitting $\Delta_{\mathrm{ex}} = E(S^{\downarrow}) + E(S^{\uparrow})$ remains constant within error bars at 600 ± 60 meV.

In the preceding section it has been shown by an analysis of the transient energy density $\varepsilon(t)$ and the line width of $S^{\uparrow}$ that within the first several hundred femtoseconds the excess energy resides in the electronic subsystem. The experimental results of time-resolved magnetic SHG and photoemission show that after an intense excitation of the electronic system the nonlinear magneto-optical signal that probes resonantly the spin polarization of the surface state
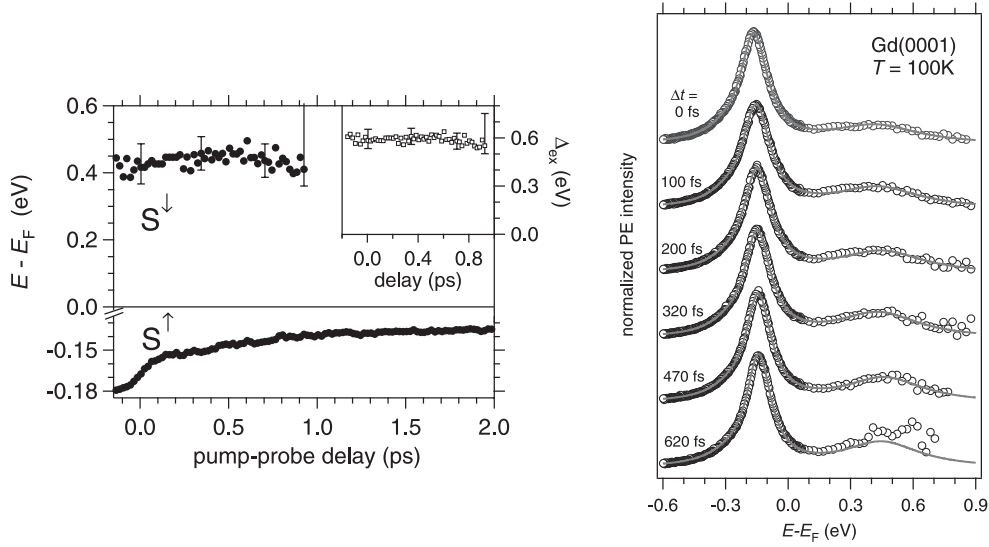
Figure 17. Right: surface contribution of TRPE spectra at different delays analysed by normalization to the non-equilibrium distribution function $f(E, t)$; see section 3.2 for details. Left: temperature levels of the occupied and unoccupied surface state components as a function of delay time with their energetic separation Δ_{ex} given in the inset. Spectra have been recorded at 100 K equilibrium temperature. Reprinted with permission from [103]. Copyright 2003 American Physical Society.

drops to half on a timescale when the excess energy still resides in the electronic system and e–e scattering dominates. Since the exchange splitting remains constant, we can safely exclude a mechanism based on a reduced Δ_{ex}, which would be expected for a Stoner-like behaviour [140]. Thus, our data on Gd(0001) indicate a prevailing of spin-mixing on the femtosecond timescale.

To develop a microscopic understanding of the ultrafast spin dynamics, we consider in the following discussion two contributions. (i) Generation of secondary electrons by means of e–e scattering in combination with transport processes and (ii) spin-flip scattering of hot electrons among spin-mixed states. Figure 18 depicts the surface electronic band structure of Gd(0001) from [98]. Panels (a) and (b) illustrate the optical excitation and generation of secondary electrons. Three excitation pathways are considered (vertical arrows). The pump pulse excites $S^\uparrow$ electrons from the occupied surface state to unoccupied bulk states, minority electrons from bulk to unoccupied surface states, and transitions between bulk states. Transitions involving the surface state redistribute spin polarization from the surface to the bulk because majority electrons are excited into bulk states or minority electrons are excited to the surface state. This redistribution is a consequence of transport effects, since the minority hole or majority electron, which is excited in the vicinity of the surface, propagates into the bulk as an electronic wavepacket with a kinetic energy and a momentum defined by its energy above E_F. In addition, as observed in TRPE directly (figure 11), the decay of hot electrons generates secondary electrons. An individual event of e–e scattering (figure 18(b)) comprises either electrons with identical spins, see e.g. processes (1) and (2), or with opposite spins, cf. (1) and (3). The latter are also termed Stoner excitations. Both relaxation channels lower the spin polarization of the surface state on a timescale < 100 fs; however, the spin polarization integrated over bulk and surface states is not altered.

The above processes could explain the initial decrease in the spin polarization of the surface state within the laser pulse duration—but not of bulk states. However, the line width of
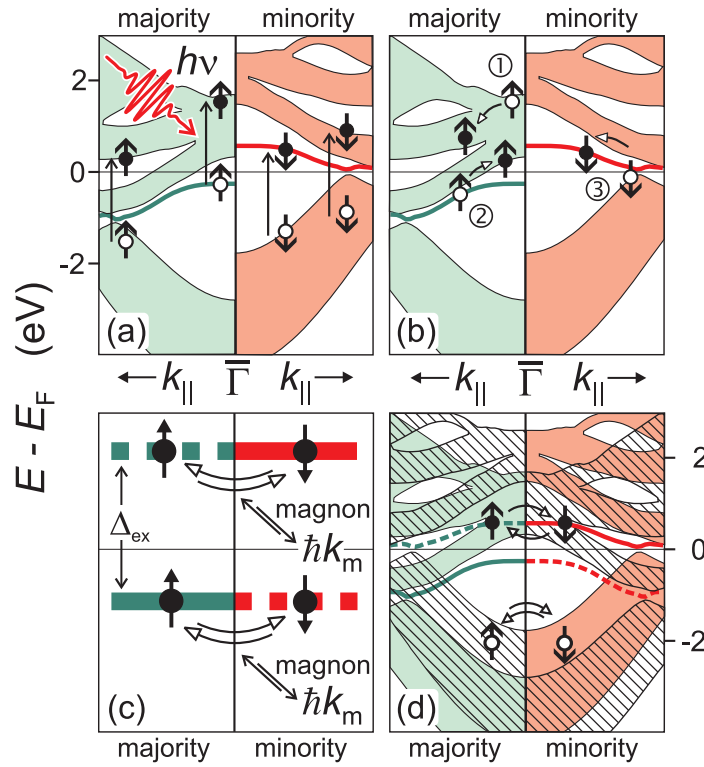
Figure 18. Majority/minority electronic band structure of the Gd(0001) surface based on reference [98]. Areas represent the projection of bulk bands into the surface plane, lines depict the exchange-split $5d_{z^2}$ surface state. The spin-mixed contributions are shown hatched in the case of bulk states and as dashed lines for the surface state. The individual panels illustrate (a) optically excited electron–hole pairs, (b) exemplary e–e scattering events, and (c), (d) electron–spin-flip scattering among spin-mixed states (shown dashed for the surface and oppositely wide hatched for the bulk). Reprinted with permission from [103]. Copyright 2003 American Physical Society.

the surface state components and the broad distribution function, which describe a maximum energy density of $\varepsilon = 1700$ K$/k_B$, imply scattering rates above 0.1 fs^{-1} (figures 13, 14, and [136]) and thus frequent scattering among surface and bulk states. This argument is corroborated by the very similar decays of the energy density observed in TRPE for s- and p-polarized probe laser pulses; see figure 12. If such redistribution and transport processes were responsible for the initial loss in the magneto-optical signal, the surface spin polarization would be restored to its initial equilibrium value by e–e scattering of surface and bulk states, i.e. within several hundred femtoseconds on the timescale of thermalization of the electron gas. Since relaxation of the laser-induced loss in spin polarization recovers much later after 40 ps (figure 16), redistribution of spin polarization among surface and bulk states does not explain the observed effect and further processes must be involved. Spin–orbit interaction has been suggested to transfer spin to orbital momentum [184, 140]. Although it cannot be excluded strictly it is unlikely to explain the observed large drop in the magneto-optical signal since electronic transitions among bulk bands and the d_{z^2} surface state do not change the orbital momentum, since both are of d character [98].

Therefore, a second contribution is invoked, which is e–e scattering accompanied by a spin-flip. As shown above, spin-mixing prevails during the first picosecond after absorption

of the pump pulse since the exchange splitting is not affected by the optical excitation. Consequently, a majority contribution at the minority state energy and a minority one for majority states is present [139], as outlined in figures 18(c) and (d). In this situation, an electron in the surface state can scatter quasi-elastically from the majority to the minority state by flipping its spin and reducing the spin polarization of the surface state (figure 18(c)). The scattering probabilities are determined in part by the density of initial and final states. Due to angular momentum conservation, such spin-flip processes are balanced by emission or absorption of a magnon, which also involves the 4f moments [52]. Consequently, the probability of the spin-flip process is governed also by the strength of e–magnon interaction. For Gd it has been established in the literature that e–magnon interaction is of the same order of magnitude as e–ph interaction [54, 152, 149, 73] and thus presents a dominant relaxation channel that occurs on the femtosecond timescale. Since in thermal equilibrium spin-mixing occurs for both bulk and surface states as reported by Maiti *et al* using spin-resolved photoemission [108], it is to be expected that e–magnon scattering in the ultrafast regime comprises both types of states as depicted in figure 18(d).

The proposed type of e–magnon scattering represents a direct pathway to reduce the spin polarization through hot electrons which store the excess energy during the collapse of the surface spin polarization. Consequently, it is expected that spin-flip scattering of electrons represents a dominant contribution in the ultrafast loss of spin polarization observed by magnetic SHG on Gd(0001).

3.5. Conclusions

By combining magneto-optical and photoemission pump–probe techniques, this study demonstrates that the ultrafast dynamics of the spin polarization and the exchange splitting do not coincide for Gd(0001). A conclusive interpretation of this phenomenon is that under non-equilibrium conditions spin-mixing dominates over Stoner behaviour. Electron–magnon interaction is proposed to facilitate electronic spin-flip scattering among surface and bulk states to explain the observed loss in the spin polarization of the surface state within the first 100 fs. We expect that the present investigation furthers a microscopic understanding of femtosecond spin dynamics and question the validity of the Stoner model under non-equilibrium conditions [140]. A theoretical description of the ultrafast spin dynamics in the excitation regime of hot electron distributions requires the inclusion of spin-flip processes. In the regime of single-electron excitations this has already been achieved for Ni [186].

The mechanism responsible for ultrafast loss of magnetization or spin polarization in exchange-split bands in ferromagnets has been investigated intensively in the last decade. However, as has been pointed out above, the underlying mechanism is still unclear. The study presented here sheds light on the responsible mechanism for one specific system. However, how far it holds for femtosecond dynamics in other systems like the itinerant ferromagnets Fe, Co, and Ni and further compounds needs to be investigated in the future. Assuming that electron–spin-flip scattering proceeds in these systems as well, the magnon excited by the spin-flip event would affect the measured magnetization, e.g. in a transient magneto-optical signal. In the case of 3d ferromagnets it is not currently clear how these two loss channels of magnetization (spin-flip process and magnon excitation) can be separated. Gd is more promising in this respect because the launched spin wave will involve the magnetic moment of 4f electrons which are localized at the ion core and energetically separated from the valence band at binding energies 9 eV below E_F. At present the occupied 4f states cannot be probed on a femtosecond timescale with technology widely available for table-top experiments but ultrashort UV light sources based on e.g. time-slicing of electron bunches in synchrotrons

or high harmonic generation in rare gas cells are very promising. To gain a comprehensive understanding of spin-dependent processes initiated by absorption of a femtosecond laser pulse, future investigations might address questions related to the ultrafast subsequent transfer processes of spin polarization among various heat baths including the lattice. Consider, e.g., energy transfer from the optically excited valence band to the heat bath of spin waves which is linked in a further interaction process by spin–lattice interaction to a sink in orbital momentum. This might induce a rotation of the sample under study along the lines of the Einstein–de-Haas effect. The current challenge in the field is to develop experiments and to study samples that are optimized for tracing these energy transfer processes over various orders in magnitude in delay times.

Promising approaches are available. Tokura and co-workers have reported systematic work on numerous compounds carried out by time-resolved linear magneto-optics defining two time regimes of ultrafast spin dynamics [120]. The initial one comprises the change during the non-radiative decay of photoexcited carriers, which is the central part of the present work. A second subsequent time interval up to 1 ns exhibits magnetic transients that depend on the magnetic anisotropy of the specific system and is thus governed by spin–orbit interaction. Koopmans *et al* propose that the spin of a valence electron can be flipped efficiently when the corresponding electron scatters at a static or dynamic defect like a phonon in an Elliot–Yafet type mechanism [95]. Beaurepaire *et al* [13] consider emitted photons as a possible sink of orbital momentum. However, the efficiency of such processes, as is well known from inverse photoemission investigations [41], is usually orders of magnitude weaker compared to scattering processes among quasiparticle excitations of the solid. Summarizing these activities it is clear that a complete understanding of spin dynamics on the femto- and picosecond timescale has not yet emerged. Thus, the complex dynamics initiated with fs laser pulses, which are based on interaction of elementary excitations of various degrees of freedom in solids, makes this field very challenging for future experimental and theoretical studies.

4. Dynamics of the coherent phonon–magnon mode

In this section coherent excitations of the lattice and the spin system on Gd(0001) at frequencies in the THz regime will be studied. The term coherent refers to well defined phase relation of the excitation with respect to time zero of the two laser pulses. The goal is a microscopic understanding of excitation, relaxation, and interaction mechanisms of such coherent lattice and spin excitations which are driven by optically excited hot electrons. The use of complementary time-resolved experimental techniques, photoelectron and optical spectroscopy, occurs to be valuable to disentangle electron–hole pair, phonon, and magnon excitations.

The approach of the present study is conceptionally different compared to investigations in thermal equilibrium, see section 1.3. A coherent optical phonon is launched by optical excitation with a femtosecond laser pulse at the Gd(0001) surface, which modulates in the time domain optical and electronic properties at the phonon frequency of 3 THz. We find a quasi-instantaneous coupling of the lattice vibration to the magnetization which oscillates at the same frequency. Thus, the coherent phonon mode facilitates insight into ultrafast spin dynamics driven by a lattice vibration.

Coherent optical phonons in solids of several terahertz frequency are well established for semiconductors and semimetals [104, 56, 31, 183, 70]. For metals coherent phonons have been observed only recently for the Gd(0001) surface [114] and for 3d transition metals by Hase *et al* [66]. Investigation of coherent spin dynamics in ferromagnets on the other hand has been strongly advanced by the demand for fast magnetic switching in data storage devices. Coherent acoustic spin waves permit switching rates of a few gigahertz, as demonstrated by

experiments using picosecond magnetic field pulses [1, 57, 172, 145]. Magnetic excitations optically driven by femtosecond laser pulses at higher frequencies up to 140 GHz have been studied [165, 17]. Optical magnon occur at frequencies of several terahertz and up to now a coherent optical magnon mode has not been observed. In the following the excitation of a coherent optical phonon–magnon mode is reported for the Gd(0001) surface and different interaction mechanisms leading to this coupled character will be discussed.

4.1. The coherent phonon–magnon mode and the coupling mechanism

An exemplary set of time-dependent optical data is given in figure 19. At the top of panel (a) the pump-induced variation of the even SH part and the linear reflectivity are displayed. Within the first 3 ps the pump-induced variation Δ_{even} presents oscillations with an amplitude of several per cent of the equilibrium value superimposed on a monotonic increase. The latter is the signature of incoherent contributions (electron–electron and electron–phonon scattering) which have been investigated by TRPE studies in section 3.2. For the linear reflectivity $\Delta R/R$ such intense oscillations are not prominent, which suggests that, owing to the surface sensitivity of SHG, the oscillating part arises at the surface. The monotonic increase is explained, like in the SHG data, by e–ph and ph–ph collisions. As seen from the bottom panel of figure 19(a), a similar behaviour is found for the spin dynamics measured by the odd SH component simultaneously. The initial drop is generated by an ultrafast loss of spin polarization due to electronic spin-flip scattering among spin-mixed states, which was discussed before in section 3.4. Relaxation back to thermal equilibrium occurs on timescales of spin–lattice relaxation and cooling within several hundred picoseconds (figure 16) [103, 166, 112]. An oscillating contribution is observed for the spin dynamics as well, which is shown after subtraction of the incoherent part for Δ_{even} and Δ_{odd} in figure 19(b) [114, 115]. Subtracting the incoherent part from the original SHG data and subsequent smoothing in a time interval below the laser pulse duration (35 fs) yields the data in figure 19(b). Their Fourier transformations, shown in the inset, exhibit identical centre frequencies for the even and odd contributions of 2.9 ± 0.3 THz, which is evidence for the coupled nature of both types of coherent excitations. The oscillations have been fitted by an exponentially damped periodic function including a frequency increasing linearly with time [25]; see section 4.3.

In the following we focus on the origin of the coherent dynamics. The phonon dispersion which has been calculated for bulk Gd [135] presents a longitudinal optical (LO) phonon at phonon momentum $q = 0$ with a frequency of 3.15 THz which is close to the one observed in our experiment. Thus, we conclude that the oscillations in $\Delta_{even}(t)$ represent a coherent optical phonon at the Gd(0001) surface excited by the femtosecond-laser pulse. In the bulk the LO phonon corresponds to vibrations of the basal planes of the hcp structure with respect to each other (Γ_{3+} mode). At the surface the LO-phonon-derived mode represents a vibration of the (0001) surface plane with respect to the underlying bulk and the interlayer distance d_{12} between the (0001) surface and the adjacent layer is modulated.

In a next step we proceed to the coherent magnetic dynamics observed in Δ_{odd}. Since this oscillating variation presents the same frequency and a constant phase shift with respect to Δ_{even}, it is concluded that these coherent lattice and spin dynamics present a coupled mode. The responsible coupling mechanism of the two subsystems is an obvious question. Spin–orbit interaction presents a possible candidate as discussed in section 1.3. However, in the case of Gd it is weak [36] and a coherent transfer of the surface vibration to the spin system cannot be explained by spin–orbit interaction. Frequencies corresponding to spin–orbit interaction are in the range of 10^{10} s^{-1}, which is far too slow to mediate the interaction between the
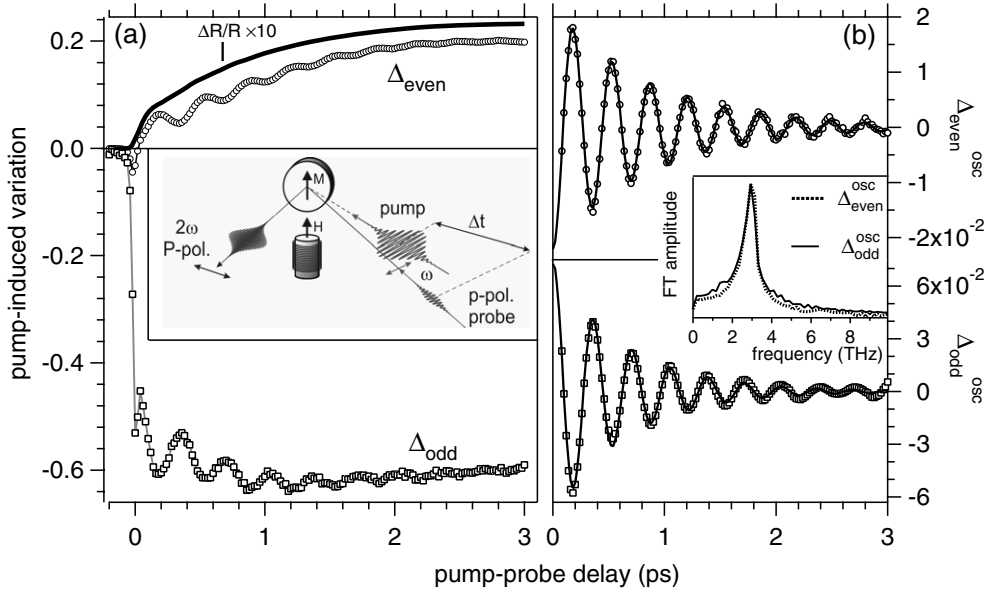
Figure 19. (a) Time dependence of the even (upper panel) and odd SH (lower panel) response as a function of pump–probe delay for a Gd(0001) film of 20 nm thickness at $T = 90$ K using 815 nm/35 fs laser pulses. Plotted are the quantities defined in equations (4)–(6). The linear reflectivity $\Delta R/R$ is displayed by the solid line. The inset shows the experimental scheme of the transversal magneto-optical geometry. (b) Coherent part of the even and odd SH fields depicted in (a) after smoothing and subtracting of the incoherent part which has been determined by the filtering procedure described in section 3.4. Solid lines represent a fit to the data (see the text). In the inset of (b), Fourier transformations of both oscillating contributions are given; after references [114, 24]. Reprinted with permission from [24]. Copyright 2003 Springer–Verlag.

lattice and the spin system coherently because the coherent mode at the surface is excited to much higher frequencies of 3×10^{12} s^{-1}. Thus, such weak spin–orbit contributions can be neglected in the discussion of the interaction mechanism of coherent optical phonons and spin excitations. However, spin–orbit coupling might be relevant for higher order contributions and slower picosecond dynamics exhibiting, e.g., precession dynamics of the magnetization.

Since the amplitude of the magnetic oscillations does not show a build-up time within the experimental time resolution and follows the lattice directly after the excitation, a stronger interaction must be responsible. First we discuss the exchange interaction J, which is determined by the wavefunction overlap of neighbouring sites to mediate the phonon–magnon coupling [114, 24]. For bulk Gd, such a dependence of J on lattice strain has been found theoretically by Blügel and co-workers [163]. Due to the d_{z^2} symmetry of the surface state one might expect that the exchange interaction along the surface normal $J_\perp$ depends on the interlayer spacing between the surface and the subsurface plane, as is the case for Gd bulk [163]. In this DFT study a change in the c/a ratio from 1.6 to 1.5 induces an increase in J of 50% and presents a pronounced variation. Such a change in c/a would ask for a dynamical variation of the lattice constant of 6% to explain the coupling in the coherent phonon–magnon mode. The observed oscillation amplitude in the variation of the spin polarization is initially 20% of the equilibrium value (figure 19) and a change of several tens of per cent is to be considered to describe the observation. By analysis of the coherent binding energy variations observed in time-resolved photoemission in combination with the DFT results (see figure 15)

we estimate the real space amplitude of the coherent phonon to be 3% of d_{12}. Thus, the phonon amplitude is one order of magnitude smaller than required for an explanation of the oscillation in the spin polarization by a coherent variation in exchange coupling. It is conceivable that at the surface the exchange coupling is more sensitive to lattice strain than in bulk. This has been tested in recent DFT calculation focusing on the surface electronic structure [105]. Within the sensitivity of these calculations, which is well within the range to find an strain-induced effect ten times larger than in bulk, the exchange splitting of the surface state remains constant. Therefore, alternative mechanisms are required to explain the coupling between the coherent phonon and magnon response. In section 3.4 we have seen that a variation in exchange splitting is not required to induce a change in the surface state's spin polarization and electron spin-flip scattering can be responsible. In fact, due to arguments given in section 3.4 the localized d_{z^2} character of the Gd(0001) surface state can favour such spin-flip processes also for coherent changes in spin polarization over dynamical variations of the exchange interaction. From a more general point of view the fact that binding of the surface layer to adjacent bulk layers involves spin-polarized orbitals suggests coupling between nuclear coordinates and the spin system. This will be investigated further and understanding of the phonon and magnon dispersion relations at the Gd(0001) surface would be very valuable for a microscopic insight.

The time-resolved investigation of the coherent mode allows us to discuss the phase of the phonon–magnon mode with respect to the instance of the optical excitation. An extrapolation of the fit function to time zero from figure 19(b) shows that both modes exhibit initially an extremal value: $\Delta_{\mathrm{even}}^{\mathrm{osc}}$ shows a minimum and $\Delta_{\mathrm{odd}}^{\mathrm{osc}}$ a maximum. As introduced above (figure 7), the optical second harmonic is generated under resonant conditions [113] with contributions from optical transitions in the majority and the minority subband, respectively. The observation of a minimum in $\Delta_{\mathrm{even}}^{\mathrm{osc}}$ at time zero is determined by the corresponding optical matrix elements in the excited state. Further conclusions from this quantity are non-trivial and would require the population of the occupied and unoccupied electronic structure and the nonlinear optical matrix elements as an input [115]. Thus the phase of $\Delta_{\mathrm{even}}^{\mathrm{osc}}$ is considered as a consequence of the electronic structure at the surface and it is not straightforward to draw conclusions from this observation. For $\Delta_{\mathrm{odd}}^{\mathrm{osc}}$, which measures the surface state spin polarization, the situation is in a first order less demanding since a difference of SHG intensities for opposite magnetization directions is analysed. The coherent contribution $\Delta_{\mathrm{odd}}^{\mathrm{osc}}$ presents an increase towards time zero and a cosine-like phase (figure 19(b)). Simultaneously, extrapolation of the phase of the oscillatory binding energy variation of the occupied surface state component suggests a stabilization of the state with respect to the transient monotonic shift of the binding towards E_F (figure 15(C), dashed line). The phase shift of π between the coherent variations in $\Delta_{\mathrm{odd}}^{\mathrm{osc}}$ and $\delta E(S^{\uparrow})$ can be explained by the following consideration. The majority state contains a tail that extends above E_F (figure 7). A shift of the state towards the band bottom leads to an increase in electron population in the majority state and thus an increase in spin polarization, in agreement with the observation. However, next to the phase the amplitude of these two oscillating quantities are to be taken into account. The binding energy variation is up to 2 meV while the spin polarization changes by a maximum of 20%. Considering the line width of the occupied surface state component of about 100 meV near the optical excitation, a binding energy change of 2 meV cannot explain a spin-polarization change of 20%. We propose that the considerable decrease in the surface state spin polarization due to spin-flip processes which amounts to half of the equilibrium value (section 3.4) enhances the coherent phenomenon considerably by the presence of electron–spin-flip channels. As already discussed in the last paragraph we expect that the efficient incoherent excitation of the magnon subsystem amplifies the oscillation in $\Delta_{\mathrm{odd}}^{\mathrm{osc}}$.

4.2. Excitation mechanism

In section 1.2 two excitation mechanisms of coherent optical phonons have been introduced. The impulsive mechanism is based on inelastic scattering of light (Raman) to excite lattice vibrations under non-resonant conditions. The displacive excitation of coherent phonons (DECP) evolves under resonant conditions where an electronic excitation is driven by the laser pulse. Responsible for the vibrations is a displacement along a nuclear coordinate of the excited state potential surface compared to the ground state potential in a Franck–Condon-like scheme illustrated by figure 3. The electronic structure in metals allows electron–hole pair excitation by absorption of optical wavelengths, which suggests a displacive excitation of coherent phonons in metals. In addition, resonant excitations are expected to dominate due to the electronic structure of Gd(0001) metal, where minority bulk electrons are excited by 1.5 eV photons to the unoccupied surface state component and majority electrons from the occupied surface state component to the unoccupied bulk state (see figure 7). The interaction responsible for the displacement of the lattice coordinate from the ground state to the excited state potential could—in a ferromagnetic sample—be of electronic or magnetic origin. In the case of an electronically driven process, the occupied or the unoccupied surface state component, or both collectively, could favour the lattice displacement. In the following the results of variations in photon energy, sample temperature, and the surface electronic structure are discussed to elucidate the excitation mechanism.

The specific electronic structure of the Gd(0001) surface suggests to vary the photon energy in order to change the ratio between excited majority holes and minority electrons in the surface state. For the smaller photon energies the excitation proceeds through the majority component, while for larger $h\nu$ the minority channel contributes in addition (see figure 7). Time-dependent data which have been obtained in the tuning range of the cavity dumped Ti:sapphire oscillator of 1.44–1.68 eV are depicted for Δ_{even} and Δ_{odd} in figure 20. The linear reflectivity $\Delta R/R$ is independent of laser wavelength. Due to the pronounced surface sensitivity of SHG, this observation confirms that the surface state, which acts as an intermediate level (see figure 7) in the nonlinear optical process, determines the spectral variation of the transient response rather than bulk states probed by $\Delta R/R$.[6]

The spectral dependence of the time-dependent even SH response, shown in the upper panel of figure 20, contains two trends for the incoherent and the coherent contribution with opposite wavelength dependences. While with decreasing photon energy the amplitude of the coherent contribution increases, the opposite holds for the incoherent part. This means that with higher photon energy incoherent contributions are excited predominantly, while for smaller $h\nu$ the coherent mode is favoured. If the electronic structure of the Gd(0001) surface is considered, one finds that with smaller photon energy the efficiency of excitations in the minority channel is reduced because the photon energy is too small to bridge the bulk and the surface minority state. The excitation probability of the majority channel presents a considerably weaker spectral dependence as it starts from the occupied surface state component into an energetically broad unoccupied bulk band (figure 7) [115].

This pronounced spectral dependence presents the following limiting cases. For the *smallest* employed photon energy of 1.44 eV the majority absorption channel is dominant. This type of excitation generates a reduction of the spin polarization (figures 16, 19) and of the electron density at the surface (figure 14). Both effects result from the fact that transitions in the minority channel are weak because the photon energy is too small to excite electrons

---

[6] Furthermore, it is seen from the wavelength variation that the phase of the oscillations is independent of the photon energy. This excludes an origin of the oscillating contributions from time-dependent variations of the optical phase ϕ between E_{odd} and E_{even} (equation (2)).
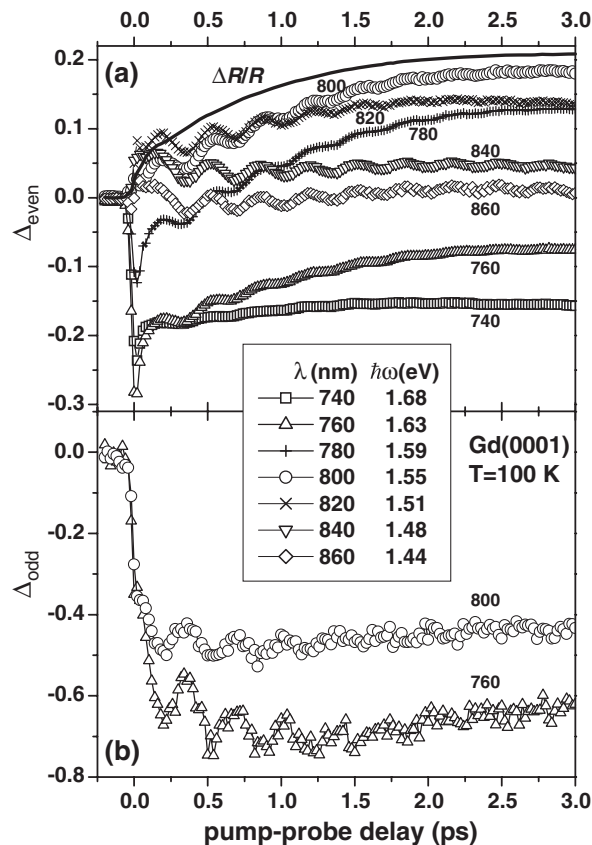
Figure 20. Pump-induced variations of SH fields during the first 3 ps for different wavelengths between 740 and 860 nm. All data are normalized to zero at negative delays according to equations (4) and (5). (a) The even SH field presents a well discernible spectral dependence of the coherent phonon contribution and of the monotonic increase after the electron system has thermalized at delays > 100 fs. The solid line represents the dependence of the linear reflectivity, which is independent of wavelength. (b) The odd field is a measure of the spin polarization at the Gd(0001) surface, which consists of coherent and incoherent contributions as well. The dominant spectral dependence here is found in the minimum value of Δ_{odd}. Reprinted with permission from [115]. Copyright 2005 Optical Society of America.

from occupied bulk to unoccupied surface states which leads to selective hole excitation in the surface state (see figure 7). The corresponding spatial redistribution of electrons and spins remains on timescales of their respective relaxation processes which are in the case of electrons given by a screening time of the order of a few femtoseconds [22, 23]. Screening of photoexcited holes within $S^{\uparrow}$ results in an effective charge redistribution in the near surface region, which is followed by an effective change of the spacing between the surface and the adjacent layer. This was suggested to be the origin of the displacive excitation of the coherent phonon–magnon mode. In the case of *larger* photon energy, the minority and majority excitation channels are both active. This means that the spin density at the surface is further reduced compared to longer wavelength because holes in the majority surface state and electrons in the minority component lower both the spin polarization at the surface. This is corroborated by the observation of a higher loss of spin polarization for the shorter wavelength seen in the bottom panel of figure 20. Considering the transient charge

distribution at the surface, electrons are excited to the unoccupied surface state component and, simultaneously, holes are created in the occupied part by excitation into unoccupied bulk states. Thus, a much weaker electron density is generated optically and a correspondingly smaller charge redistribution is required for screening the excited region near the surface, which leads to a less efficient lattice displacement and, thus, a weaker amplitude of the coherent mode.

Alternatively to this charge-driven mechanism, we consider that the pump-induced variation of the surface spin polarization, which is lowered upon laser excitation by more than 50% (figure 16), drives the coherent mode. For a ferromagnetic system the screened ion potential is spin dependent, as has been shown by analysis of the extended x-ray absorption fine structure of Gd [176]. In this work a considerable spin-dependent electron density that screens the ion potential is observed, which results in an effective spin dependence of the ion potential. The author concludes an energy difference of the potential for opposite spin directions of the order of half of the exchange interaction. This means that the ion lattice is coupled to the spin system. It would be well conceivable that the coupled coherent phonon–magnon mode is generated by the laser-induced change of the surface spin polarization induced by spin-flip scattering as presented in section 3.4.

One way to systematically vary the spin polarization in the surface and to investigate the effect on the coherent dynamics is to increase the temperature up to the Curie temperature of 293 K. In figure 21 the magnetic SH contrast which measures the spin polarization of the surface state is plotted as a function of temperature. Over a broad temperature range a quasi-linear behaviour is observed, which changes close to the Curie temperature T_C into critical behaviour, as discussed in section 3.1. Open symbols represent the initial amplitude of Δ^{osc} for even and odd contributions. An excitation mechanism driven by the spin polarization is expected to depend on this quantity. Since the exchange interaction, which is the reason for the unbalanced excitation of electrons and holes in the surface as discussed above, varies with temperature [19], see figure 8, a temperature dependence is also expected for the charge-driven mechanism. To decide whether the phonon excitation is spin or electron driven, the temperature-dependent spin polarization of the surface state and of its exchange splitting is compared (figure 8). At a first glance, oscillation amplitudes and magnetic contrast follow the same trend and vanish near the Curie point, which suggests the consideration of the spin polarization to explain the excitation probability of the coherent mode. However, it is observed that the oscillatory amplitude in the even SHG contribution is clearly finite above T_C. Comparing the oscillation amplitude with the exchange splitting for, e.g., 100 K and T_C reveals that the oscillation amplitude decreases by about one order while the exchange splitting is reduced only to half. Thus, there is no simple linear relation between these properties. The conclusion from the temperature-dependent work is that either there are contributions to the excitation mechanism from the spin and the charge degrees of freedom with different respective temperature-dependent variations, or, alternatively, an excitation probability of an electronically driven phonon that scales nonlinearly with the exchange splitting can be considered for an explanation of the experimental observation.

One further step has been taken to analyse the excitation process with contributions of all three relevant degrees of freedom (charge, lattice, and spin) by investigating the effect on the coherent dynamics generated by a change of the electronic structure through a controlled variation of the chemical composition of the surface. This has been achieved by preparing Y overlayers on the Gd surface. Like Gd, Y presents an hcp structure at very similar lattice constant, which deviates only by 0.5% from Gd, favouring epitaxial growth on Gd(0001). Furthermore, it exhibits the same electronic valence structure but lacks 4f electrons, which leads to a $5d_{z^2}$ surface state of Y(0001) at the Fermi level, however without exchange splitting
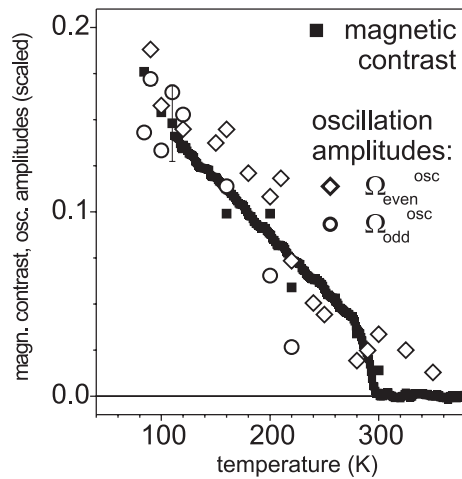
Figure 21. Temperature-dependent magnetic contrast $\left(I^{\uparrow} - I^{\downarrow}\right) / \left(I^{\uparrow} + I^{\downarrow}\right)$ (solid squares) and initial amplitudes of the oscillatory lattice and spin excitations (open symbols); from [24].

since Y is diamagnetic. Consequently, the resonant SHG process which is required for the pump–probe investigation of the coherent mode is expected to occur also for Y(0001) while the exchange splitting vanishes. Therefore, preparation of a few yttrium monolayers (MLs) on Gd(0001) allows us to change the electronic structure from an exchange-split situation of bare Gd(0001) to a non-magnetic surface at Y/Gd(0001). This behaviour has been monitored in photoelectron spectroscopy under equilibrium conditions carried out at the synchrotron BESSY II at a photon energy of 36 eV [114]. Figure 22(b) shows the evolution of the occupied surface state component from Gd(0001) to 3 ML Y(0001)/Gd(0001). A single ML of Y results in a change in the electronic structure, where Y induces a second surface contribution shifted towards the Fermi level while the Gd(0001) surface state remains. After deposition of 3 ML Y the Gd state has almost completely vanished, and the Y(0001) surface state has shifted to energies above E_F. This is concluded from the asymmetric peak shape, which is terminated at high energies by the Fermi–Dirac distribution. Under comparable conditions time-resolved SHG studies have been carried out where the Y thickness has been monitored by a quartz crystal balance. As depicted in figure 22, it is observed that the oscillating contribution to the transient even SHG signal is reduced by the first ML of Y and almost completely damped by 3 ML Y. From this experiment we conclude that a simple surface state is not sufficient for the excitation of the coherent phonon but the exchange splitting turns out to be a prerequisite.

This subsection is concluded by pointing out that various experimental indications are in favour of an excitation process of the coherent mode that is driven by an optically induced electron redistribution among surface and bulk states of Gd(0001). However, in particular the temperature dependence of the oscillation amplitudes asks for a contribution to the excitation process from optically generated changes in the spin polarization of the surface state. Thus, it is likely that at temperatures below T_C a cooperative action of spin and charge degrees of freedom leads to the coherent lattice excitation at 3 THz observed by time-resolved nonlinear optics and photoemission. To answer the question of whether the coherent spin dynamics are primarily driven by hot electrons that excite a coherent phonon coupled to the spin system, or whether the coherent spin dynamics occur in response to the optical excitation of a exchange-split electronic structure followed by the phonon system, is challenging, not only because of the non-equilibrium state where it occurs, but of the various degrees of freedom that
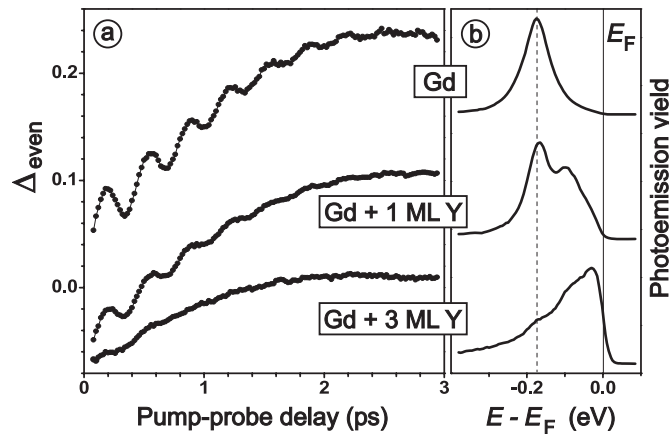
Figure 22. (a) Quenching of the oscillatory even SHG contribution by Y overlayers measured at 800 nm laser wavelength. (b) Photoemission spectra of bare Gd(0001) and covered by nominally 1 and 3 ML coverage (photon energy 36 eV). From [114].

participate in the excitation, coupling, and relaxation process. A future effort should comprise theoretical investigation of the magnon and phonon dispersion relation at the Gd(0001) surface. Furthermore, exploration of the series of heavy rare earth elements might shed some light on these open questions because of the very similar elastic properties combined with pronounced variations in the 4f magnetism and the magnon spectrum.

4.3. Damping of the coherent mode and coupling to the bulk

Relaxation of the coherent spin–lattice mode can proceed by various scattering processes. On the one hand a coherent mode can interact inelastically with the thermalized heat baths of electrons, phonons, or magnons. In addition, elastic scattering can occur at defects. The experimentally observed damping can generally be described as a sum of the depopulation rate (inelastic scattering) and the pure dephasing rate (elastic scattering) [99, 128]. For coherent phonons a detailed understanding of relaxation channels has been developed by Hase and co-workers for the case of Bi [68, 71, 67]. Temperature-dependent damping times of the coherent A_{1g} mode of Bi agree with a decay of a coherent optical phonon into two acoustical modes which are symmetric with respect to the Λ point at half the energy of the optical mode [71]. Moreover, a systematic variation of the point-defect density of the same phonon mode has been reported [68]. Compared to these coherent phonons in semimetals, the relaxation processes of the coherent spin–lattice mode on the Gd(0001) surface involves the following additional relaxation pathways.

  (i) The spin system adds scattering channels between phonons and magnons.
 (ii) It is to be expected that decay of the coherent spin mode proceeds through processes corresponding to the ones contributing to the decay of coherent phonons (magnon–defect, magnon–magnon, and magnon–phonon scattering).
(iii) Since Gd is metallic, coherent phonons (or spin waves) can decay by excitation of an electron–hole pair through ph–e (magnon–e) interaction.
(iv) At the Gd(0001) surface the optical mode is expected to have a lower frequency due to the break of symmetry.

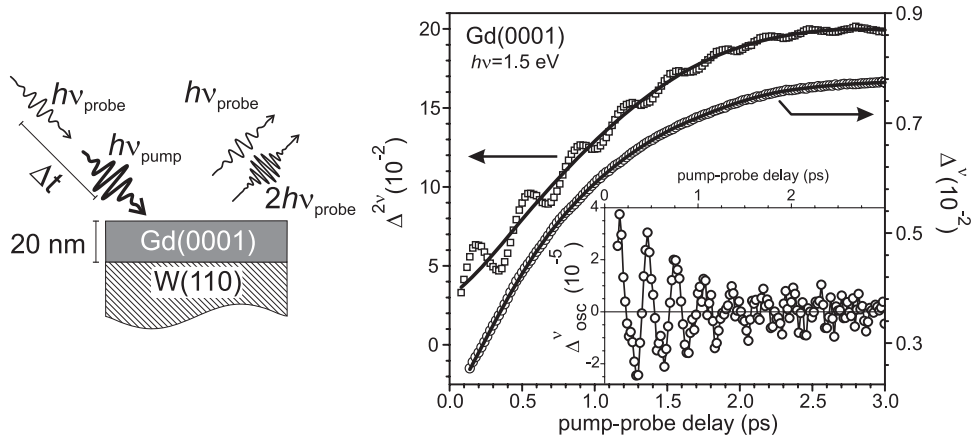**Figure 23.** Pump-induced variations of linear (circles, right axis) and second harmonic (squares, left axis) reflectivity within the first 3 ps after excitation by the pump pulse, measured for a 20 nm Gd(0001) film on W(110) at 90 K. Solid lines indicate the incoherent contributions in $\Delta^{2\nu}$ and Δ^{ν}. The inset shows the oscillating part in linear reflectivity obtained by subtraction of the incoherent background. Note the difference in axis scale between Δ^{ν} and $\Delta^{\nu}_{\text{osc}}$. On the left a schematic diagram of the simultaneous linear and nonlinear optical experiment is given. Reprinted with permission from [25]. Copyright 2004 American Physical Society.

A separation of all these contributions is demanding and as a first step temperature-dependent damping rates are important to discuss. These studies are currently underway and are not reviewed here. However, an analysis of the SH and linear reflectivity pump–probe data in combination with the time-resolved photoemission data (section 3) facilitate insight into the damping processes of the coherent surface mode.

The dispersion of the optical phonon mode in bulk Gd, which has been calculated [135], suggests a resonant interaction of the surface mode at 3 THz with the bulk LO phonon. Therefore, the coherent mode which has been shown to be excited at the Gd(0001) surface through the exchange-split surface state in section 4.2 is expected to drive a coherent vibration in the bulk layers adjacent to the surface.

Thus, the processes responsible for the damping of the coherent mode at the surface are involved. The present study demonstrates contributions which have to be considered, but with regard to the multifaceted relaxation pathways outlined above a complete understanding is still on its way to being developed. As a starting point for the experimental investigation, nonlinear SH and linear optical pump–probe studies have been carried out simultaneously as illustrated in the left panel of figure 23. By this approach the decay of excitation in the bulk mode and in the surface can be compared directly and separation of the coherent and incoherent contributions allow some understanding of the damping.

Figure 23 shows the evolution of the even SH yield $\Delta^{2\nu}_{\text{even}}(t)$ and the linear reflectivity $\Delta^{\nu}(t)$ within 3 ps after arrival of the pump pulse according to equations (4)–(6). The initial optical excitation of electrons forms a non-equilibrium distribution which thermalizes within several hundred femtoseconds (figure 10) by electron–electron scattering. Subsequently, electron–phonon interaction leads to energy transfer to the lattice system, which finally results in equilibration between electrons and phonons as shown in section 3.2. This is also indicated by the saturation in the transient optical data (linear and nonlinear reflectivity, figure 23). For later times (>3 ps, not shown) the equilibrated hot lattice and the electron system cool by heat diffusion into less excited regions of the sample [112]. This process is governed by the temperature gradient in the Gd film and its heat conductivity [112].

This section discusses the damping of the coherent phonon, which occurs during the first three picoseconds after excitation. Note that delays > 100 fs are analysed, where the existence of an electron temperature can be assumed (cf figure 10). The significant increase in pump-induced changes (15% for $\Delta_{even}^{2\nu}$ and 0.6% in the case of Δ_{even}^{ν}) is characteristic for the non-equilibrium excited state during which electrons and phonons have not yet reached a common temperature [79, 50]. The linear reflectivity has been fitted by an exponential increase and the resulting rise time of 0.88(2) ps characterizes the energy transfer rate from hot electrons to the lattice[7]. The observed very similar timescales of saturation of the incoherent contributions to the second harmonic and to the linear reflectivity indicate that electron–phonon interaction is of comparable strength at the surface and in the bulk[8].

The incoherent part of both SH and linear reflectivity is superimposed by oscillations, damped within picoseconds, which are recognized easily in the SH data (see figure 23). Although not evident at a first glance, such oscillations are also present in the linear reflectivity, but their initial amplitude is about 10^3 times smaller. As shown in the inset of figure 23, the damped oscillations can easily be identified after subtraction of the exponential function fitted to $\Delta^{\nu}(t)$. To evaluate the frequencies, incoherent and coherent contributions were separated. The results are shown in figure 24 by open circles for the second harmonic (a) and the linear reflectivity (b). Fourier transformations of both coherent contributions are presented in figure 24(c). The centre frequencies are determined to be $\Omega_s = 2.9(1)$ THz for the surface and $\Omega_b = 3.3(1)$ THz for the bulk. Note that these values average over the time span of 3 ps. Two different frequencies are observed, evidencing that the vibrations arise from atoms in two different surroundings, like surface and bulk. Furthermore, both Fourier transformations displayed in figure 24(c) exhibit asymmetric peak shapes. While the linear reflectivity spectrum shows a spectral weight toward higher frequencies, the second harmonic data show the opposite trend. One is tempted to attribute the higher bulk value to a stronger bonding of the ion cores compared to those in the surface layer. Interestingly, we find in these frequency shifts a dynamical evolution.

The temporal evolution of coherent vibrations detected in the surface and the bulk has been analysed by two different ways. First, we fitted the data shown in figures 24(a) and (b) by a phenomenological expression using a damped oscillation at frequency Ω with a linearly shifting frequency $\langle \partial\Omega/\partial t \rangle /2 = b$ and a damping time τ:

$$\Delta_{osc}(t) = A_0\, e^{-t/\tau} \cos[(\Omega t + bt^2 + \phi)2\pi]. \tag{14}$$

Figure 24 shows fits to the data with the following parameters: $\Omega_s = 2.80(5)$ THz, $\partial\Omega_s/\partial t = +0.17(1)$ THz ps^{-1}, $\tau_s = 0.86(5)$ ps for the surface and $\Omega_b = 3.44(5)$ THz, $\partial\Omega_b/\partial t = -0.12(5)$ THz ps^{-1}, $\tau_b = 0.9(1)$ ps for the bulk oscillations, respectively. The linear frequency chirp is required to fit the data, as illustrated by the dashed line in the inset of figure 24. Such a dynamical variation in frequency might be related to the asymmetric line shapes observed in the Fourier transformations (figure 24(c)) and in agreement with literature reports on coherent phonons excited in Bi [70] and Si [69]. To test whether a linear shift is appropriate for a description the pump–probe data have been fitted within a time window of

---

[7] Implicitly energy transfer to the magnon heat bath is considered hereby as well, by assuming the same timescale for electron–magnon and electron–phonon interaction [54, 152, 149, 73]. A separation of the magnon heat bath would be valuable. For this purpose measurements in the vicinity of the Curie point might be promising because the specific heat strongly changes in this regime, which will influence the relaxation dynamics of hot electrons.

[8] The transient energy density analysed in TRPE by s- and p-polarized probe beams (figure 12) suggested significant, although small, differences in the e–ph interaction in the Gd surface and the bulk. Optical data are in this respect less quantitative because the nonlinear and linear optical responses do not necessarily depend linearly on the transient energy density.
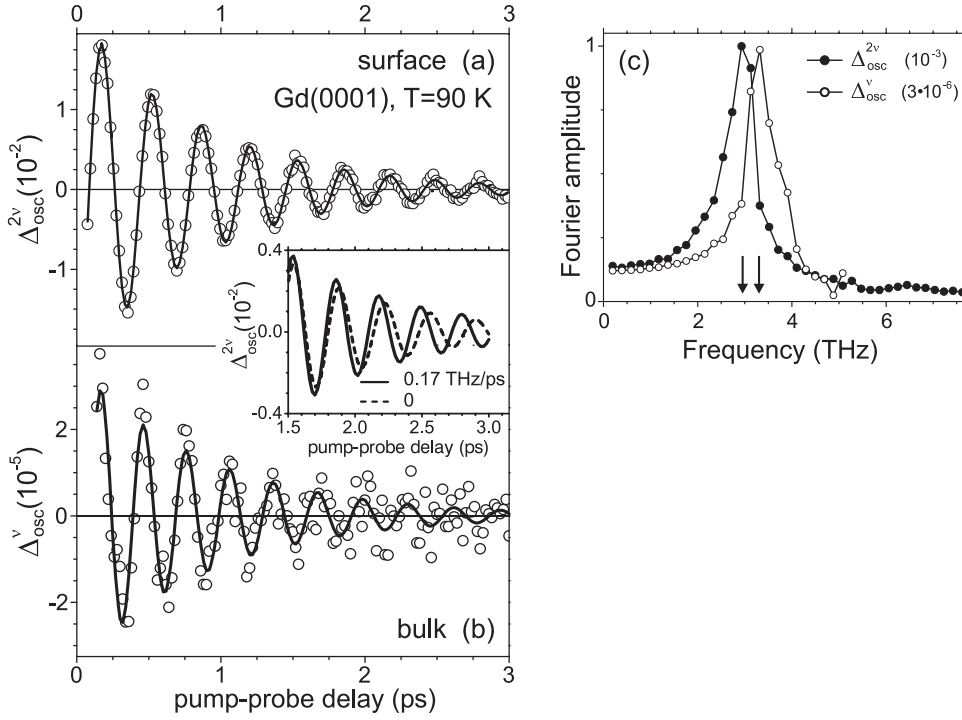
Figure 24. Experimental data (circles) of $\Delta_{osc}^{2\nu}$ (a) and Δ_{osc}^{ν} (b) after subtraction of incoherent contributions to the transient signals. Solid lines represent fits to a phenomenological function (see text). In the inset fits by equation (14) with $\partial\Omega_s/\partial t = 0$ (dashed line) and with a frequency shift of 0.17 THz ps^{-1} (solid line, also shown in panel (a)) are compared. Only the latter reproduces the data up to 3 ps. (c) Fourier transformations of the coherent contributions to the transient optical data, which exhibits different frequencies for surface (●) and bulk (○) lattice vibrations, as indicated by arrows. Both peaks show a clear asymmetry, with the bulk mode tending to higher frequencies, while the surface mode has a tail in the opposite direction. This corresponds to different frequency shifts for both vibrations (see the text). Reprinted with permission from [25]. Copyright 2004 American Physical Society.

0.4 ps centred at delay time t by the following function.

$$\Delta_{osc}(t') = \left(A(t) + \frac{\partial A(t)}{\partial t}(t - t')\right) \cos\left(2\pi(\Omega(t)t' + \phi(t))\right), \tag{15}$$

with A and Ω as adjustable parameters and the derivative and the phase ϕ defined by the values of A, Ω and ϕ within current and previous segment positions. By shifting the time window in 0.1 ps steps, the parameters were obtained as a function of time and are displayed in figure 25. It is apparent that Ω_s is characterized by a blue shift of about 9% within the first 2 ps. Although at later delays the uncertainty of the data increases due to progressive damping, the blue shift saturates around 3 ps. Poorer statistics in Δ_{osc}^{ν} results in fewer data points. Nevertheless, it is evident that the bulk frequency shows a red shift. The grey lines represent the linear frequency chirp $\langle\partial\Omega/\partial t\rangle$ as analysed above (figure 25, equation (15)). Since both chirps for the surface and for the bulk follow the variation of frequencies in figure 25, both methods of analysis are in quantitative agreement. Thus, we find that surface and bulk frequencies converge within error bars to a common value at $t > 2$ ps. This asymptotic value is in good agreement with theoretical results for the Γ_{3+}-mode near the Γ-point [135] shown as a horizontal dashed line. The oscillation amplitudes for surface ($A_{even}^{2\nu}$) and bulk (A^{ν}) are shown as a function of
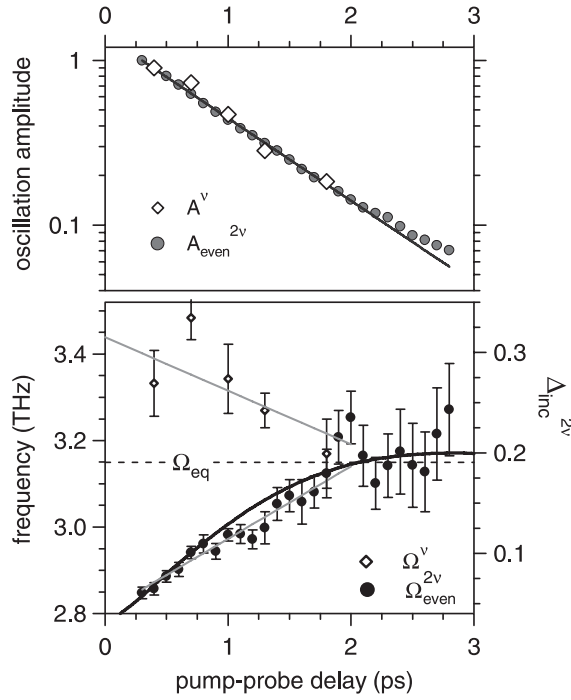
Figure 25. Top panel: transient amplitudes of the linear reflectivity A^ν and of the even oscillatory SHG contributions $A_{even}^{2\nu}$, which are determined by description of the oscillatory components by equation (15) on a logarithmic scale. The initial amplitudes have been normalized to unity. Lower panel: surface and bulk phonon frequencies (left axis) as a function of pump–probe delay. Grey lines represent the linearly chirped frequency determined by fitting the data with equation (14). The black solid line depicts, for comparison, the incoherent contribution of the SH intensity, which is an effective measure for the decay of hot electrons (right axis); adapted from [25].

delay in the top panel of figure 25. The amplitudes can be fitted well using an exponential decay as shown by solid lines. Decay times for bulk ($\tau_b = 0.87(5)$ ps) and for the surface $\tau_s = 0.86(5)$ ps agree with each other. Thus, the responsible processes do not have to be discussed separately for bulk and surface.

From the incoherent part of the transient linear reflectivity we concluded above (figure 23) that the transfer of excess energy from hot electrons to the phonon system is characterized by a characteristic time of $0.88(2)$ ps (see also section 3). This value matches well with the damping time of coherent phonons of 0.86(2) and 0.9(1) ps derived (equation (14)) from $\Delta_{osc}^{2\nu}$ and Δ_{osc}^ν, respectively. This agreement suggests that the attenuation of coherent surface and bulk vibrations is governed by inelastic phonon–electron scattering. A further contribution might be scattering of the coherent lattice motion with incoherent phonons. A comparison of typical damping times for coherent phonons at similar equilibrium temperatures in semimetals [39], metals [66], and materials exhibiting metal–insulator transitions [126, 40], shows that in metals the damping of coherent phonons is about an order of magnitude faster. This is explained by scattering of coherent phonons with electrons, which is efficient in metals because electron–hole pairs can be excited by the energy of a phonon, while in semiconductors and semimetals partial or total energy gaps restrict this process. Likewise, the short decay time of the coherent phonon on the Gd(0001) surface of about 1 ps is attributed to phonon–electron scattering.

Interaction of the coherent phonon with thermal phonons or magnons will also contribute on longer timescales but has not been identified so far.

A striking feature of the non-equilibrium dynamics of coherent phonons in Gd(0001) is the large opposite frequency shift as a function of delay time for surface and bulk vibrations (figure 25). Blue-shift of coherent phonon frequencies as a function of delay time is a well known feature [69, 70, 33] which has been attributed to cubic anharmonicity. However, a red-shift with delay time has not yet been observed. Obviously, these opposite frequency shifts for bulk and surface contributions are related. We exclude an origin of these dynamical shifts in frequencies from anharmonicities; for details see [25]. As discussed in the following, we observe here an effect of the non-equilibrium electron distributions, which differ for surface and bulk states, on the ion potentials.

In section 4.2 it has been discussed that the coherent mode at the surface is excited by displacement of the surface plane, driven by absorption of photons and electron–hole pair excitation in the Gd(0001) surface state. Since the surface atoms are bound to the subsurface atoms, any displacement of the surface layer along the surface normal is transferred to neighbouring bulk layers (monitored by $\Delta_{\mathrm{osc}}^{\nu}$) within a certain penetration depth before the initial displacement is diminished. We suggest that the vibration observed in linear reflectivity originates from such coupling of the surface vibration to deeper layers. This is corroborated by the fact that in the bulk only coherent phonons of A_1-symmetry can be excited by light [157], but the frequency of about 3 THz measured with linear reflectivity disagrees with the expected A_1-frequency of 2.3 THz [135]. Excitation of the observed vibration with a frequency close to the Γ_{3^+}-bulk mode must therefore originate from the surface displacement. Note that vibrations of the surface (0001)-plane and the corresponding bulk planes should differ due to (i) different coordination (12 in the bulk, nine in the surface) and (ii) the coupling strength varies for bulk and surface due to a 3% inward relaxation of the surface along the c-axis in equilibrium [29]. This is confirmed by the observation of two different frequencies at the early delay times. In order to understand the transient variation of frequencies we consider the temporal evolution of the screened ion potential generated by the relaxation of hot electrons excited by the femtosecond-laser pulse.

Absorption of the pump pulse leads to holes in the occupied part of the surface state and to electrons in the unoccupied part (figure 7). Since the majority component is situated closer to E_{F} than the minority component, holes live longer than electrons (see section 3.4, [136]). Moreover, hole generation is favoured over electron excitation for the surface state at the employed photon energy (figure 20). Thus, the electron density at the surface is reduced by the optical excitation. Since the enhanced electron density at the surface leads in equilibrium to an inward relaxation [29], the laser-induced reduction of electron density at the surface will reverse this effect and will induce a transient increase in the distance d_{12} in the potential minimum from the surface. This is corroborated by the phase and the sign of the coherent binding energy variations observed in time-resolved photoemission spectroscopy (figure 15). The resulting reduction in bond strength along [0001] leads to a force on the ions along the surface normal and initiates the coherent lattice motion discussed before.

Scattering of electrons in the hot electron gas establishes an electron temperature within 100 fs (section 3.2). Subsequently, energy transfer to the lattice occurs through electron–phonon interaction. In the respective time regime < 3 ps the force on the ions recedes since the electron density determines the screened ion potential, which in turn defines the vibration frequency. We conclude therefore that the transient variation of the potential is responsible for the changes observed in the coherent phonon frequency Ω_{s}. The formation of an equilibrium among electrons and phonons occurs within the same time interval in which the frequency variation saturates. The incoherent electron dynamics are investigated in time-

resolved photoemission directly (section 3) and in the optical experiment—although more indirectly—by the incoherent contributions to the time evolution of the optical signals. We included in figure 25, bottom, the incoherent part of the pump-induced variation in the even SHG signal (black line). Clearly, the change of the surface frequency coincides with the evolution of the scaled incoherent contribution, which provides evidence for the proposed scenario that the frequency shift is caused by the transient non-equilibrium of the electron density at the surface. Conversely, the red shift observed for the bulk frequency in the transient linear reflectivity is attributed to the reversed variation of electron density in the bulk, which continuously decreases within the first 3 ps, i.e. during e–ph equilibration.

5. Outlook and conclusions

The femtosecond time-resolved investigations of the ferromagnetic metal surface Gd(0001) comprise non-equilibrium many-particle dynamics of electron, lattice, and spin degrees of freedom. The presented time domain approach facilitated a detailed investigation of elementary processes and interactions that couple electronic excitations to further quasi-particle excitations like phonons and magnons.

The combined experimental approach of time-resolved photoemission and nonlinear magneto-optics demonstrated that the exchange splitting of the $5d_{z^2}$ surface state remains constant during the first picosecond after optical excitation. This is remarkable since the maximum transient energy density in the electronic system is typically given by $\varepsilon = 1700$ K$/k_B$, characterizing a non-equilibrium regime where interaction of hot particles with each other has to be taken into account. Relaxation of this excess energy occurs by scattering of excited electrons with electrons, phonons, and magnons. The spin polarization of the surface state has been measured independently in a nonlinear optical pump–probe experiment employing resonant second harmonic generation at the Gd(0001) surface. Assuming that the nonlinear magneto-optical signal is proportional to the magnetic moment, the spin polarization of the surface state is reduced within the experimental resolution of 50 fs to half. This phenomenon is explained by the loss of spin polarization of the state due to spin-mixing of the surface state on the ultrafast timescale. This implies spin-flip scattering among hot electrons in the surface state, among surface and bulk states and most likely also among bulk states, which occurs within the first 100 fs. Spin-flip scattering of valence electrons is facilitated by interaction with the magnon system that includes the 4f electrons with their magnetic moments localized at the ion core. Little is known about restrictions on available timescales imposed by this process, which asks for further investigations. The proposed description explains the loss of spin polarization on a femtosecond timescale without violation of angular momentum conservation but by coupling the 5d spin system to the 4f states. The current challenge in the field of femto- and picosecond spin dynamics is to determine the sequence of non-equilibrium processes that lead to equilibration of magnetic subsystems like the itinerant valence band magnetism in Gd compared to the total spin system that includes the 4f magnetic moments. However, this requires experimental techniques to study the dynamics in the 4f system in addition to the valence band. The current development of femtosecond UV and x-ray sources will allow time-resolved experiments employing these higher photon energies to monitor the spin dynamics in the 4f states in comparison to the valence band. To disentangle the processes important in ultrafast spin dynamics the investigation of rare earth systems could be more promising than the 3d transition metal ferromagnets. The latter have been studied in various laboratories during the last decade [94] and a separation of individual processes during the first picoseconds has proven to be difficult. As a complementary approach, our work will be extended to other rare earth systems like Tb and Dy to test and improve the microscopic

understanding. If femtosecond-light sources that allow pump–probe experiments to address the spins in the 4f electrons become feasible, a separation of electron dynamics that occur in the conduction band and spin dynamics in the 4f levels will become available from an experimental point of view.

In addition, the Gd(0001) surface state presents a coherent dynamics which has been attributed to optical excitation of a coherent phonon–magnon mode. The frequency observed in the time-resolved SHG is near 3 THz, which is explained by a coherent phonon at the surface derived from the bulk LO mode. The magnetic SH signal also presents an oscillatory contribution which is found at the same frequency. This observations asks for interaction between lattice and spin excitations which are faster than the oscillation period of 330 fs. Based on a theoretical result that shows a constant exchange splitting in the surface state for different interlayer spacings, an interlayer dependence of the exchange interaction can be excluded as the responsible coupling mechanism. By time-resolved photoemission it was found that the occupied surface state component also exhibits a periodic change in the binding energy at the frequency observed in SHG pump–probe studies. This shows unambiguously that the SHG oscillations are generated by a 'breathing' of the electronic structure of the surface. Considering the spin-polarized character of the surface state which is responsible for bonding of the surface layer to the bulk it can be expected that variation of the interlayer spacing influences the spin polarization and vice versa. The temperature-dependent behaviour of the oscillation amplitude shows a pronounced increase for temperatures below the Curie temperature of Gd, which favours a magnetic effect to be the initial driving force of the coupled coherent phonon–magnon mode. Further theoretical investigation that considers the dynamics of the Gd(0001) surface is underway. An interesting question to be investigated in the future is the role of the 5d–4f exchange interaction that might transfer the coherent spin excitation observed in the $5d_{z^2}$ state to the 4f magnetic moments. In this respect, a direct time-resolved probe of the 4f spin dynamics would be important and new femtosecond VUV and XUV light sources like time-slicing of electron bunches in synchrotrons or high harmonic generation in gas cells are very promising. Furthermore, it is of interest whether the described principles of phonon–magnon interaction are general, i.e. apply to other systems as well. In a first step further heavy lanthanide surfaces will be studied employing the presented approach. More generally, it is not only challenging to address the ultrafast dynamics of the spin system. Characteristic timescales and processes of electron correlation can be studied in pump–probe experiments as well, which suggests to explore superconductors, systems with Mott instabilities, or charge density waves in the future.

References

[1] Acremann Y, Back C H, Buess M, Portmann O, Vaterlaus A, Pescia D and Melchior H 2000 *Science* **290** 492

[2] Aeschlimann M, Bauer M, Pawlik S, Knorren R, Bouzerar G and Bennemann K H 2000 *Appl. Phys.* A **71** 485

[3] Aeschlimann M, Bauer M, Pawlik S, Weber W, Burgermeister R, Oberli D and Siegmann H C 1997 *Phys. Rev. Lett.* **79** 5158

[4] Aharony A 2000 *Introduction to the Theory of Ferromagnetism* 2nd edn (New York: Oxford University Press)

[5] Allen P B 2001 *Phys. Rev.* B **63** 214410

[6] Anisimov S I, Kapeliovich B L and Perel'man T L 1974 *Sov. Phys.—JETP* **39** 375

[7] Arenholz E, Navas E, Starke K, Bazmgarten L and Kaindl G 1995 *Phys. Rev.* B **51** 8211

[8] Arnold C S and Pappas D P 2000 *Phys. Rev. Lett.* **85** 5202

[9] Ashcroft N W and Mermin N D 1976 *Solid State Physics* 1st edn (Fort Worth: Harcourt)

[10] Aspelmeier A, Gerhardter F and Baberschke K 1994 *J. Magn. Magn. Mater.* **132** 22–30

[11] Bargheer M, Zhavoronkov N, Gritsai Y, Woo J C, Kim D S, Woerner M and Elsaesser T 2004 *Science* **306** 1771

[12] Beaurepaire E, Merle J-C, Daunois A and Bigot J-Y 1996 *Phys. Rev. Lett.* **76** 4250

[13] Beaurepaire E, Turner G M, Harrel S M, Beard M C, Bigot J-Y and Schmuttenmaer C A 2004 *Appl. Phys. Lett.* **84** 3465

[14] Bennemann K H 1998 *Non-Linear Optics in Metals* (Oxford: Clarendon)

[15] Berger L 2001 *J. Appl. Phys.* **89** 5521

[16] Bigot J-Y, Guidoni L, Beaurepaire E and Saeta P N 2004 *Phys. Rev. Lett.* **93** 077401

[17] Bigot J-Y, Guidoni L and Halté V 2002 *Ultrafast Phenomena XIII* (*Springer Series in Chemical Physics*) (Berlin: Springer) p 398

[18] Bihlmayer G and Blügel S 2006 private communication

[19] Bode M, Getzlaff M, Heinze S, Pascal R and Wiesendanger R 1998 *Appl. Phys.* A **66** S121

[20] Boger K, Weinelt M and Fauster T 2004 *Phys. Rev. Lett.* **92** 126803

[21] Bonn M, Denzler D N, Funk S, Wolf M, Wellershoff S-S and Hohlfeld J 2000 *Phys. Rev.* B **61** 1101

[22] Borisov A, Sánchez-Portal S, Diez Muiño R and Echenique P M 2004 *Chem. Phys. Lett.* **387** 95

[23] Borisov A, Sánchez-Portal S, Diez Muiño R and Echenique P M 2004 *Chem. Phys. Lett.* **393** 132

[24] Bovensiepen U 2006 *Appl. Phys.* A **82** 395

[25] Bovensiepen U, Melnikov A, Radu I, Krupin O, Starke K, Wolf M and Matthias E 2004 *Phys. Rev.* B **69** 235417

[26] Brorson S D, Fujimoto J G and Ippen E P 1987 *Phys. Rev. Lett.* **59** 1962

[27] Brown P J, Deportes J, Givord D and Ziebeck K R A 1982 *J. Appl. Phys.* **53** 1973

[28] Bucksbaum P H 2004 *Science* **306** 1691

[29] Bylander D M and Kleinman L 1994 *Phys. Rev.* B **50** 1994

[30] Capellmann H (ed) 1987 *Metallic Magnetism* (Berlin: Springer)

[31] Chang Y M, Xu L and Tom H W K 1997 *Phys. Rev. Lett.* **78** 4649

[32] Cheng T K, Vidal J, Zeiger H J, Dresselhaus G, Dresselhaus M S and Ippen E P 1991 *Appl. Phys. Lett.* **59** 1923

[33] Cheng T K, Vidal J, Zeiger H J, Ippen E P, Dresselhaus G and Dresselhaus M S 1993 *Appl. Phys. Lett.* **62** 1901

[34] Cho G C, Kütt W and Kurz H 1990 *Phys. Rev. Lett.* **65** 764

[35] Cinchetti M, Sanchez-Albaneda M, Hoffmann D, Roth T, Wüstenberg J-P, Krauss M, Andreyev O, Schneider H C, Bauer M and Aeschlimann M 2006 *Phys. Rev. Lett.* **97** 177201

[36] Colarieti-Tosti M, Simak S I, Ahuja R, Nordström L, Eriksson O, Åberg D, Edvardsson S and Brooks M S S 2003 *Phys. Rev. Lett.* **91** 157201

[37] Coqblin B 1977 *The Electronic Structure of Rare-Earth Metals and Alloys* (London: Academic)

[38] Dan'kov S Yu, Tishin A M, Pecharsky V K and Gschneidner K A Jr 1998 *Phys. Rev.* B **57** 3478

[39] Dekorsy T, Cho G C and Kurz H 2000 *Coherent Phonons in Condensed Media* (*Springer Topics in Applied Physics* vol 76) (Berlin: Springer)

[40] Demsar J, Forró L, Berger H and Mihailovic D 2002 *Phys. Rev.* B **66** R041101

[41] Donath M 1994 *Surf. Sci. Rep.* **20** 251

[42] Donath M, Dowben P A and Nolting W 1998 *Magnetism and Electronic Correlations in Local Moment Systems: Rare Earth Elements and Compounds* (Singapore: World Scientific)

[43] Donath M, Gubanka B and Passek F 1996 *Phys. Rev. Lett.* **77** 5138

[44] Drude P 1900 *Ann. Phys., Lpz.* **1** 566

[45] Drulis H and Drulis M 1991 *Magnetic Properties of Rare Earth Elements, Alloys and Compounds* (*Landolt-Börnstein New Series* vol 3/19d1) (Berlin: Springer)

[46] Echenique P M, Berndt R, Chulkov E V, Fauster Th, Goldmann A and Höfer U 2004 *Surf. Sci. Rep.* **52** 219

[47] Echenique P M, Pitarke J M, Chulkov E V and Rubio A 2000 *Chem. Phys.* **251** 1

[48] Fann W S, Storz R, Tom H W K and Bokor J 1992 *Phys. Rev.* B **46** 13592

[49] Farle M, Baberschke K, Stetter U, Aspelmeier A and Gerhardter F 1993 *Phys. Rev.* B **47** 11571
[50] Del Fatti N, Viosin C, Achermann M, Tzortzakis S, Christofilos D and Valleé F 2000 *Phys. Rev.* B **61** 16956
[51] Fauster T and Steinmann W 1995 *Two-Photon Photoemission Spectroscopy of Image States* (*Electromagnetic Waves: Recent Developments in Research* vol 2) (Amsterdam: Elsevier)
[52] Fedorov A V, Valla T, Liu F, Johnson P D, Weinert M and Allen P B 2002 *Phys. Rev.* B **65** 212409
[53] Fiebig M, Fröhlich D, Krichevtsov B B and Pisarev R V 1994 *Phys. Rev. Lett.* **73** 2127
[54] Fulde P and Jensen J 1983 *Phys. Rev.* B **27** 4085
[55] Gahl C, Bovensiepen U, Frischkorn C and Wolf M 2002 *Phys. Rev. Lett.* **89** 107402
[56] Garrett G A, Albrecht T F, Whitaker J F and Merlin R 1996 *Phys. Rev. Lett.* **77** 3661
[57] Gerrits Th, van den Berg H A M, Hohlfeld J, Bär L and Rasing Th 2002 *Nature* **418** 509
[58] Gilton T L, Cowin J P, Kubiak G D and Hamza A V 1990 *J. Appl. Phys.* **68** 4802
[59] Greber T, Kreutz T J and Osterwalder J 1997 *Phys. Rev. Lett.* **79** 4465
[60] Grimvall G 1981 *The Electron–Phonon Interaction in Metals* (Amsterdam: North-Holland)
[61] Groeneveld R H M, Sprik R and Lagendijk A 1995 *Phys. Rev.* B **51** 11433
[62] Guidoni L, Beaurepaire E and Bigot J-Y 2002 *Phys. Rev. Lett.* **89** 017401
[63] Gusev V E and Wright O B 1998 *Phys. Rev.* B **57** 2878
[64] Haas C W and Callen H B 1963 *Ferromagnetic Relaxation and Resonance Line Width* (*Magnetism* vol 1) (New York and London: Academic)
[65] Haight R 1995 *Surf. Sci. Rep.* **21** 275
[66] Hase M, Ishioka K, Demsar J, Ushida K and Kitajima M 2005 *Phys. Rev.* B **71** 184301
[67] Hase M, Ishioka K, Kitajima M and Ushida K 2003 *Appl. Phys. Lett.* **82** 3668
[68] Hase M, Ishioka K, Kitajima M, Ushida K and Hishita S 2000 *Appl. Phys. Lett.* **76** 1258
[69] Hase M, Kitajima M, Constantinescu A M and Petek H 2003 *Nature* **426** 51
[70] Hase M, Kitajima M, Nakashima S and Mizoguchi K 2002 *Phys. Rev. Lett.* **88** 067401
[71] Hase M, Mizoguchi K, Harima H, Nakashima S and Sakai K 1998 *Phys. Rev.* B **58** 5448
[72] Hase M, Mizoguchi K, Harima H, Nakashima S, Tano A, Sakai K and Hanygo M 1996 *Appl. Phys. Lett.* **69** 2474
[73] Hatta E, Sasaki T, Svistunov V M, Belogolovskii M A, Chernyak O I, Khachaturov A I and Gerasimenko A Y 2001 *J. Phys. Soc. Japan* **70** 1865
[74] Hengsberger M, Purdie D, Segovia P, Garnier M and Baer Y 1999 *Phys. Rev. Lett.* **83** 592
[75] Hill R W, Collocott S J, Gschneidner K A Jr and Schmidt F A 1987 *J. Phys. F: Met. Phys.* **17** 1867
[76] Hillebrands B and Ounadjela K (ed) 2002 *Spin Dynamics in Confined Magnetic Systems 1* (*Springer Topics in Applied Physics* vol 83) (Berlin: Springer)
[77] Hillebrands B and Ounadjela K (ed) 2003 *Spin Dynamics in Confined Magnetic Systems 2* (*Springer Topics in Applied Physics* vol 87) (Berlin: Springer)
[78] Hohlfeld J, Matthias E, Knorren R and Bennemann K H 1997 *Phys. Rev. Lett.* **78** 4861
[79] Hohlfeld J, Wellershoff S-S, Güdde J, Conrad U, Jähnke V and Matthias E 2000 *Chem. Phys.* **251** 237
[80] Hong J and Mills D L 2000 *Phys. Rev.* B **62** 5589
[81] Hüfner S 1995 *Photoelectron Spectroscopy* (*Springer Series in Solid-State Science* vol 82) (Berlin: Springer)
[82] Jacobsson P and Sundqvist B 1989 *Phys. Rev.* B **40** 9541
[83] Javey A, Guo J, Paulsson M, Wang Q, Mann D, Lundstrom M and Dai H 2004 *Phys. Rev. Lett.* **92** 106804
[84] Jensen J 1971 *Int. J. Magn.* **1** 271
[85] Jensen J and Houmann J G 1975 *Phys. Rev.* B **12** 320
[86] Ju G, Hohlfeld J, Bergman B, van den Veerdonk R J M, Mryasov O N, Kim J-Y, Wu X, Weller D and Koopmans B 2004 *Phys. Rev. Lett.* **93** 197403
[87] Kaganov M I, Lifshitz I M and Tanatarov L V 1957 *Sov. Phys.—JETP* **4** 173
[88] Kant C H, Kurnosikov O, Filip A T, Swagten H J M and de Jonge W J M 2003 *J. Appl. Phys.* **93** 7528
[89] Kaveh M and Wisner N 1984 *Adv. Phys.* **33** 257
[90] Kiselev S I, Sankey J C, Krivorotov I N, Emley N C, Schoelkopf R J, Buhrman R A and Ralph D C 2003 *Nature* **425** 380
[91] Kittel C 1963 *Quantum Theory of Solids* (New York: Wiley)
[92] Kliewer J, Berndt R, Chulkov E V, Silkin V M, Echenique P M and Crampin S 2000 *Science* **288** 1399
[93] Koehler W C, Child H R, Nicklow R M, Smith H G, Moon R M and Cable J W 1970 *Phys. Rev. Lett.* **24** 16
[94] Koopmans B 2003 *Spin Dynamics in Confined Magnetic Structures II* (*Springer Topics in Applied Physics* vol 87) (Berlin: Springer)
[95] Koopmans B, Ruigroky J J M, Dalla Longa F and de Jonge W J M 2005 *Phys. Rev. Lett.* **95** 267207
[96] Koopmans B, van Kampen M, Kohlhepp J T and de Jonge W J M 2000 *Phys. Rev. Lett.* **85** 844
[97] Kreuzer S, Moser J, Wegscheider W, Weiss D, Bichler M and Schuh D 2002 *Appl. Phys. Lett.* **80** 4582
[98] Kurz Ph, Bihlmayer G and Blügel S 2002 *J. Phys.: Condens. Matter* **14** 6353
[99] Laubereau A and Kaiser W 1978 *Rev. Mod. Phys.* **50** 607

[100] Li D, Pearson J, Bader S D, McIlroy D N, Waldfried C and Dowben P A 1995 *Phys. Rev.* B **51** 13895
[101] Lisowski M, Loukakos P A, Bovensiepen U, Stähler J, Gahl C and Wolf M 2004 *Appl. Phys.* A **78** 165
[102] Lisowski M, Loukakos P A, Bovensiepen U and Wolf M 2004 *Appl. Phys.* A **79** 739
[103] Lisowski M, Loukakos P A, Melnikov A, Radu I, Ungureanu L, Wolf M and Bovensiepen U 2005 *Phys. Rev. Lett.* **95** 137402
[104] Lobad A I and Taylor A I 2001 *Phys. Rev.* B **64** R180301
[105] Loukakos P A, Lisowski M, Bihlmayer G, Blügel S, Wolf M and Bovensiepen U 2007 *Phys. Rev. Lett.* at press
[106] Lyo I-W and Plummer E W 1988 *Phys. Rev. Lett.* **60** 1558
[107] Madelung O 1978 *Introduction to Solid State Theory* (Berlin: Springer)
[108] Maiti K, Malagoli M C, Dallmeyer A and Carbone C 2002 *Phys. Rev. Lett.* **88** 167205
[109] Matsumoto Y and Watanabe K 2006 *Chem. Rev.* **106** 4234
[110] Matzdorf R 1998 *Surf. Sci. Rep.* **30** 153
[111] McDougall B A, Balasubramaniam T and Jensen E 1995 *Phys. Rev.* B **51** 13891
[112] Melnikov A, Bovensiepen U, Radu I, Krupin O, Starke K, Matthias E and Wolf M 2004 *J. Magn. Magn. Mater.* **272–276** 1001
[113] Melnikov A, Krupin O, Bovensiepen U, Starke K, Wolf M and Matthias E 2002 *Appl. Phys.* B **74** 723
[114] Melnikov A, Radu I, Bovensiepen U, Krupin O, Starke K, Matthias E and Wolf M 2003 *Phys. Rev. Lett.* **91** 227403
[115] Melnikov A, Radu I, Bovensiepen U, Starke K, Wolf M and Matthias E 2005 *J. Opt. Soc. Am.* B **22** 204
[116] Merschdorf M, Kennerknecht C, Willig K and Pfeiffer W 2002 *New J. Phys.* **4** 95
[117] Miller A D, Bezel I, Gaffney K J, Garrett-Roe S, Liu S H, Szymanski P and Harris C B 2002 *Science* **298** 1163
[118] Myers E B, Ralph D C, Katine J A, Louie R N and Buhrman R A 1999 *Science* **285** 867
[119] Nolting W, Borgiel W, Dose V and Fauster Th 1989 *Phys. Rev.* B **40** 5015
[120] Ogasawara T, Ohgushi K, Tomioka Y, Takahashi K S, Okamoto H, Kawasaki M and Tokura Y 2005 *Phys. Rev. Lett.* **94** 087202
[121] Oppeneer P M and Liebsch A 2004 *J. Phys.: Condens. Matter* **16** 5519
[122] Paggel J J, Miller T and Chiang T-C 1998 *Phys. Rev. Lett.* **81** 5632
[123] Pan R-P, Wei H D and Shen Y R 1989 *Phys. Rev.* B **39** 1229
[124] Passek F, Donath M, Ertl K and Dose V 1995 *Phys. Rev. Lett.* **75** 2746
[125] Paul O M 1990 Determination of energy-resolved inelastic mean free paths of electrons with spin-polarized secondary and Auger electron spectroscopy *PhD Thesis* Swiss federal institute of technology, Zürich, Diss. ETH No. 9210
[126] Perfetti L, Loukakos P A, Lisowski M, Bovensiepen U, Berger H, Biermann S, Cornaglia P S, Georges A and Wolf M 2006 *Phys. Rev. Lett.* **97** 067402
[127] Petek H and Heinz A F (ed) 2000 *Chemical Physics* vol 251 (Amsterdam: North-Holland)
[128] Petek H and Ogawa S 1997 *Prog. Surf. Sci.* **56** 239
[129] Petek H, Weida M J and Nagano H 2000 *Science* **288** 1402
[130] Pines D and Nozieres P 1966 *The Theory of Quantum Liquids* (New York: Benjamin)
[131] Platow W, Anisimov A N, Dunifer G L, Farle M and Baberschke K 1998 *Phys. Rev.* B **58** 5611
[132] Plihal M and Mills D L 1994 *Phys. Rev.* B **50** 13480
[133] Plihal M and Mills D L 1998 *Phys. Rev.* B **58** 14407
[134] Plihal M, Mills D L and Kirschner J 1999 *Phys. Rev. Lett.* **82** 2579
[135] Rao R R and Menon C S 1974 *J. Phys. Chem. Solids* **35** 425
[136] Rehbein A, Wegener D, Kaindl G and Bauer A 2003 *Phys. Rev.* B **67** 033403
[137] Reinert F, Nicolay G, Schmidt S, Ehm D and Hüfner S 2001 *Phys. Rev.* B **63** 115415
[138] Rethfeld B, Kaiser A, Vicanek M and Simon G 2002 *Phys. Rev.* B **65** 214303
[139] Rex S, Eyert V and Nolting W 1999 *J. Magn. Magn. Mater.* **192** 529
[140] Rhie H-S, Dürr H A and Eberhardt W 2003 *Phys. Rev. Lett.* **90** 247201
[141] Rhie H-S, Dürr H A and Eberhardt W 2006 *Appl. Phys.* A **82** 9
[142] Ridley B K 1988 *Quantum Processes in Semiconductors* (Oxford: Oxford University Press)
[143] Schmidt A B, Pickel M, Wiemhöfer M, Donath M and Weinelt M 2005 *Phys. Rev. Lett.* **95** 107402
[144] Scholl A, Baumgarten L, Jacquemin R and Eberhardt W 1997 *Phys. Rev. Lett.* **79** 5146
[145] Schumacher H W, Chappert C, Crozat P, Sousa R C, Freitas P P, Miltat J, Fassbender J and Hillebrands B 2003 *Phys. Rev. Lett.* **90** 017201
[146] Schüßler-Langeheine C, Weschke E, Mazumdar C, Meier R, Grigoriev A Y, Kaindl G, Sutter C, Abernathy D, Grübel G and Richter M 2000 *Phys. Rev. Lett.* **84** 5624
[147] Shah J 1983 *Ultrafast Spectroscopy of Semiconductors and Semiconductor Nanostructures* 2nd edn (Berlin: Springer)

[148] Shen Y R 1984 *The Principles of Nonlinear Optics* (New York: Wiley)
[149] Skriver H L and Mertig I 1990 *Phys. Rev.* B **41** 6553
[150] Slonczewski J C 1996 *J. Magn. Magn. Mater.* **159** L1
[151] Sokolowski-Tinten K, Blome C, Blums J, Cavalleri A, Dietrich C, Tarasevitch A, Uschmann I, Förster E,
        Kammler M, Horn von Högen M and von der Linde D 2003 *Nature* **422** 287
[152] Sondhelm S A and Young R C 1985 *J. Phys. F: Met. Phys.* **15** L261
[153] Stamps R L, Camley R E, Hillebrands B and Güntherodt G 1993 *Phys. Rev.* B **47** 5072
[154] Stewart J Q 1928 *Phys. Rev.* **11** 100
[155] Sun Z, Chuang Y-D, Fedorov A V, Douglas J F, Reznik D, Weber F, Aliouane N, Argyriou D N, Zheng H,
        Mitchell J F, Kimura T, Tokura Y, Revcolevschi A and Dessau D S 2006 *Phys. Rev. Lett.* **97** 056401
[156] Tangney P and Fahy S 1999 *Phys. Rev. Lett.* **82** 4340
[157] Tangney P and Fahy S 2002 *Phys. Rev.* B **65** 054302
[158] Thiele J-U, Buess M and Back C H 2004 *Appl. Phys. Lett.* **85** 2857
[159] Töben L, Gundlach L, Ernstorfer R, Eichberger R, Hannappel T, Willig F, Zeiser A, Förstner J, Knorr A,
        Hahn P H and Schmidt W G 2005 *Phys. Rev. Lett.* **94** 067601
[160] Tober E D, Ynzunza R X, Westphal C and Fadley C S 1996 *Phys. Rev.* B **53** 5444
[161] Tsang T-W E, Gschneidner K A Jr, Schmidt F A and Thome D K 1985 *Phys. Rev.* B **31** 235
[162] Tsoi M, Sun J Z and Parkin S S P 2004 *Phys. Rev. Lett.* **93** 036602
[163] Turek I, Kudrnovsky J, Bihlmayer G and Blügel S 2003 *J. Phys.: Condens. Matter* **15** 2771
[164] Valla T, Fedorov A V, Johnson P D and Hulbert S L 1999 *Phys. Rev. Lett.* **83** 2085
[165] van Kampen M, Josza C, Kohlhepp J T, LeClair P, Lagae L, de Jonge W J M and Koopmans B 2002 *Phys. Rev.
        Lett.* **88** 227201
[166] Vaterlaus A, Beutler T and Meier F 1991 *Phys. Rev. Lett.* **67** 3314
[167] Vigren D T and Liu S H 1972 *Phys. Rev.* B **5** 2719
[168] von der Linden W, Donath M and Dose V 1993 *Phys. Rev. Lett.* **71** 899
[169] Ward L 1998 *Optical Constants of Eight Rare Earth Elements* (*Handbook of Optical Constants of Solids* vol 3)
        (San Diego, CA: Academic)
[170] Watanabe K, Takagi N and Matsumoto Y 2002 *Chem. Phys. Lett.* **366** 606
[171] Watanabe K, Takagi N and Matsumoto Y 2004 *Phys. Rev. Lett.* **92** 057401
[172] Weber H, Riesen S and Siegmann H C 2001 *Science* **291** 1015
[173] Wegner D, Bauer A and Kaindl G 2006 *Phys. Rev.* B **73** 165415
[174] Weinelt M 2002 *J. Phys.: Condens. Matter* **14** R 1099
[175] Weinelt M, Kutschera M, Fauster T and Rohlfing M 2004 *Phys. Rev. Lett.* **92** 126801
[176] Wende H 2004 *Rep. Prog. Phys.* **67** 2105
[177] Weschke E, Schüssler-Langeheine C, Meier R, Fedorov A V, Starke K, Hübinger F and Kaindl G 1996 *Phys.
        Rev. Lett.* **77** 3415
[178] White C T and Todorov T N 1998 *Nature* **393** 240
[179] Wolf M and Aeschlimann M 1998 *Phys. Bl.* **54** 145
[180] Wolf M, Hotzel A, Koesel E and Velic D 1999 *Phys. Rev.* B **59** 5926
[181] Wolf M, Koesel E and Hertel T 1996 *Phys. Bl.* **54** R5295
[182] Zangwill A 1988 *Physics at Surfaces* (Cambridge: Cambridge University Press)
[183] Zeiger H J, Vidal J, Cheng T K, Ippen E P, Dresselhaus G and Dresselhaus M S 1992 *Phys. Rev.* B **45** 768
[184] Zhang G, Hübner W, Beaurepaire E and Bigot J-Y 2002 *Spin Dynamics in Confined Magnetic Structures 1*
        (*Springer Topics in Applied Physics* vol 83) (Berlin: Springer)
[185] Zhang G P and Hübner W 2000 *Phys. Rev. Lett.* **85** 3025
[186] Zhukov V P, Chulkov E V and Echenique P M 2004 *Phys. Rev. Lett.* **93** 096401